

On variability and spectral distortion of the fluorescent iron lines from black-hole accretion discs

Andrzej Niedźwiecki^{1*} and Piotr T. Życki²

¹*Łódź University, Department of Physics, Pomorska 149/153, 90-236 Łódź, Poland*

²*Nicolaus Copernicus Astronomical Center, Bartycka 18, 00-716 Warsaw, Poland*

Accepted 2007 November 16. Received 2007 October 23; in original form 2007 January 12

ABSTRACT

We investigate properties of iron fluorescent line arising as a result of illumination of a black hole accretion disc by an X-ray source located above the disc surface. We study in details the light-bending model of variability of the line, extending previous work on the subject.

We indicate bending of photon trajectories to the equatorial plane, which is a distinct property of the Kerr metric, as the most feasible effect underlying reduced variability of the line observed in several objects. A model involving an X-ray source with a varying radial distance, located within a few central gravitational radii around a rapidly rotating black hole, close to the disc surface, may explain both the elongated red wing of the line profile and the complex variability pattern observed in MCG–6-30-15 by *XMM-Newton*.

We point out also that illumination by radiation which returns to the disc (following the previous reflection) contributes significantly to formation of the line profile in some cases. As a result of this effect, the line profile always has a pronounced blue peak (which is not observed in the deep minimum state in MCG–6-30-15), unless the reflecting material is absent within the innermost 2–3 gravitational radii.

Key words: accretion, accretion disc – relativity – galaxies: active – X-rays: binaries – X-rays: individual: MCG–6-30-15

1 INTRODUCTION

Broad iron lines observed from many black hole systems most likely originate from the innermost regions of an accretion disc and their profiles are shaped by gravitational redshift and Doppler shifts. Modelling of the lines observed in several objects requires strongly enhanced fluorescent emission from a few gravitational radii (e.g., Wilms et al. 2001, Fabian et al. 2002, Miller et al. 2002, Miller et al. 2004; see review in Reynolds & Nowak 2003), which in turn indicates that a primary source of hard X-ray emission must also be located close to the black hole. Thus, both the primary and reflected emission should be subject to strong gravity effects. These effects are also tentatively considered as an explanation of the complex variability pattern characterising radiation reflected from disc, including the iron line, and the primary hard X-ray continuum emission. Namely, weak variability of the reflected component, uncorrelated with the variability of the primary emission, has been reported in a number of sources (e.g., Vaughan & Fabian 2004; see review in Fabian & Miniutti 2005). This is contrary to ex-

pectations from a simple geometrical model of a hard X-ray source located close to the reflecting disc, where a strict correlation between variations of the primary and reflected emission should be observed.

Fabian & Vaughan (2003) first argued that such a reduced variability may be explained by relativistic effects, in particular by light bending and focusing the primary emission towards the accretion disc. Qualitatively, variations of the reflected emission should be much weaker as changes of the height of the X-ray source cause variations of its observed luminosity at infinity, while changes of the flux received by the disc (enhanced by the gravitational focusing; e.g., Matt et al. 1992; Martocchia & Matt 1996; Petrucci & Henri 1997) are much weaker. However, for a static primary source located on the symmetry axis, the illuminating radiation is focused into the innermost part of the disc and the reflected emission is subject to similar light bending as the primary. As a result, similar variability characterises the primary and reflected emission, at least for observers with low inclination angles.

Miniutti et al. (2003) and Miniutti & Fabian (2004) have developed further this model to include rotation of the primary source around the axis and the resulting beaming

* e-mail: niedzwiecki@uni.lodz.pl

of its emission toward outer regions of the disc. Then, variations of the reflected emission are reduced because of the more extended region it is produced. Predictions of their model are found to be consistent with observations of black-hole systems, e.g. by Miniutti et al. (2003), Miniutti, Fabian & Miller (2004), Fabian et al. (2004). However, a number of important effects were not systematically studied. In particular, a specific pattern of motion of a primary source is assumed (including both location relative to the symmetry axis and azimuthal motion) but it is not discussed how strongly the resulting properties depend on these assumptions. For example, corotation of the primary source with the disc is assumed by Miniutti & Fabian (2004), which is likely close to the disc surface, but at most approximate at high latitudes. As the azimuthal motion of the primary source relative to the disc may affect significantly the reflected emission (see e.g. Reynolds & Fabian 1997), it is not clear whether predictions of this model are specific to the underlying assumptions or generic to models involving the light bending.

In this paper we systematically analyse the light bending model, concentrating on strong gravity effects. We neglect some other effects which may contribute to the original variability problem, for example, ionization of the disc surface (Nayakshin & Kazanas 2002). We focus here on the iron $K\alpha$ line; an analysis of reflected emission including the Compton reflected radiation will be presented in our next paper. We study in details a number of geometrical scenarios of the source location and motion. We point out certain inadequacies in the original computations of Miniutti & Fabian (2004), and how they influence their quantitative results. We find also a novel scenario in which reduction of the line variability follows directly from properties of photon transfer in the Kerr metric. Namely, we find that a source located close to the disc surface, with a varying radial distance from a Kerr black hole, gives rise to both an approximately constant illumination of the surrounding disc and a very strong variability of the primary emission observed at infinity. Some aspects of variability in similar models have been considered recently e.g. by Czerny et al. (2004) and Pecháček et al. (2005), however, these studies considered only emission emerging locally from the region under the source. On the other hand, we find that transfer of primary emission to more distant regions of the disc is crucial for variability effects in such a model.

We concentrate on low inclination objects, with application to Seyfert 1 galaxies in mind. Obviously, the Doppler shifts are more pronounced at high inclinations, but observational studies of high inclination objects are less advanced, either because they are obscured (as Seyfert 2 galaxies), or because the studies on dynamical time scale are not possible (as in stellar mass black hole systems). Furthermore, we consider only emission averaged over at least an orbital period. Effects resulting from varying azimuthal location of an off-axis source, with respect to observer, are studied, e.g., in Ruszkowski (2000), Yu & Lu (2000) and Goyder & Lasenby (2004).

In Section 3 we analyse various physical effects relevant to formation of relativistic line profiles and variability effects; in Section 4 we apply our results to a Seyfert 1 galaxy MCG-6-30-15 which is the best studied object with clear signatures of strong gravity effects.

2 MODEL DESCRIPTION

We consider an accretion disc, surrounding a Kerr black hole, irradiated by X-rays emitted from an isotropic point source (hereafter referred to as the source of primary emission). The black hole is characterised by its mass, M , and angular momentum, J . We use the Boyer-Lindquist (BL) coordinate system $x^i = (t, R, \theta, \phi)$. We also make use of locally non-rotating (LNR) frames (Bardeen, Press & Teukolsky 1972), which are particularly convenient for studying processes in the Kerr geometry (in the Schwarzschild metric the LNR frame is equivalent to the rest frame of a local static observer).

The following dimensionless parameters are used in the paper

$$r = \frac{R}{R_g}, \quad a = \frac{J}{cR_g M}, \quad \Omega = \frac{d\phi}{dt}, \quad (1)$$

where $R_g = GM/c^2$ is the gravitational radius and $\hat{t} = ct/R_g$. In most cases we compute spectra for $a = 0.998$. To illustrate effects which are uniquely related to black hole rotation, we compare in some cases spectra for $a = 0.998$ with spectra for corresponding models in the Schwarzschild metric ($a = 0$).

We assume that a geometrically thin, neutral, optically thick disc is located in the equatorial plane of the Kerr geometry. The radial coordinate in the disc plane is denoted by r_d . For distances larger than the radius of the marginally stable circular orbit, r_{ms} ($= 1.23$ and 6 for $a = 0.998$ and $a = 0$, respectively) we assume a circular motion of matter forming the disc, with Keplerian angular velocity (Bardeen et al. 1972),

$$\Omega_K(r_d) = \frac{1}{a + r_d^{3/2}}. \quad (2)$$

We take into account emission from matter extending down to the event horizon. In most cases (except for model S_0 , see below) we assume that matter free falls within r_{ms} . We strictly follow Cunningham (1975) in description of velocity field at $r_d < r_{ms}$ in models assuming the free fall. In most cases we assume the outer radius of the emitting region in the disc $r_{out} = 600$, but we compute also spectra for smaller r_{out} for comparison with previous studies.

We assume that the primary X-ray emission is generated isotropically in the source rest frame. We neglect transversal or radial motion of the source, $u^\theta = 0$ and $u^r = 0$, but take into account azimuthal motion. The motion is characterised by $V \equiv v^\phi/c$, where v^ϕ is the azimuthal velocity with respect to the LNR frame. To illustrate influence of V we compare models with $V = 0$, which allows to separate effects due to gravity from kinematic effects, and $V = 0.5$, which is a typical value of orbital velocity in the innermost regions.

Inclination of the rotation axis of the black hole to the line of sight is given by $\mu_{obs} \equiv \cos \theta_{obs}$. Most results (except for these shown in Fig. 12) presented in this paper are for $\mu_{obs} = 0.85$, which is typical for objects presumably affected by strong gravity (in particular, MCG-6-30-15 and Narrow Line Seyfert 1 galaxies).

2.1 Monte Carlo

We use a Monte Carlo method, involving a fully general relativistic (GR) treatment of photon transfer in the Kerr space-time, to find spectra of primary emission and Fe line observed by a distant observer. A large number of photons are generated from the primary source with isotropic distribution of initial directions in the source rest frame. Lorentz transformation, with relative velocity V , yields photon energy, E_{in} , and momentum components (in the BL coordinate directions), $p_{(r)}$, $p_{(\theta)}$ and $p_{(\phi)}$, in the LNR frame. These, in turn, yield constants of motion (cf. eq. (10) in Niedźwiecki (2005))

$$E_{\text{inf}} = \left(\frac{\Delta\Sigma}{A}\right)^{1/2} E_{\text{in}} + \left(\frac{A}{\Sigma}\right)^{1/2} \omega \sin\theta p_{(\phi)} c \quad (3)$$

$$\lambda \equiv \frac{Lc}{E_{\text{inf}} R_g} = \left(\frac{A}{\Sigma}\right)^{1/2} \frac{\sin\theta p_{(\phi)} c}{E_{\text{inf}}} \quad (4)$$

$$\eta \equiv \frac{Qc^2}{E_{\text{inf}}^2 R_g^2} = \frac{p_{(\phi)}^2 c^2}{E_{\text{inf}}^2} \Sigma + \cos^2\theta \left(\frac{\lambda^2}{\sin^2\theta} - a^2 \right), \quad (5)$$

where E_{inf} is the photon energy at infinity, Q is the Carter's constant, L is the component of angular momentum parallel to the black hole rotation axis, and

$$\Delta = r^2 - 2r + a^2, \quad \Sigma = r^2 + a^2 \cos^2\theta, \\ A = (r^2 + a^2)^2 - a^2 \Delta \sin^2\theta, \quad \omega = 2ar/A. \quad (6)$$

A photon trajectory is fully determined by λ and η .

For each photon, equations of motion are solved to find whether the photon crosses the event horizon, hits the disc surface or escapes directly to distant observer. Photon emission rate, yielding normalisation of directly observed and illuminating fluxes (see below), is corrected by time dilation factor,

$$g_t \equiv \frac{dt_s}{dt} = \left(\frac{\Sigma\Delta}{A}\right)^{1/2} (1 - V^2)^{1/2}, \quad (7)$$

where dt_s is the time interval in the source rest frame.

For a photon hitting the disc surface, at r_d , we find incidence angle and energy, E_{disc} , in the disc rest frame. Then, for $E_{\text{disc}} > 7.1$ keV, we generate an iron $K\alpha$ photon, with energy 6.4 keV, emerging from the disc. The relative weight of the Fe photon is related to the initial energy and direction of an incident photon by the quasi-analytic formula [eqs. (4-6)] from George & Fabian (1991). We modify the original formula by multiplying it by a factor of 1.3 to account for different elemental abundances (we use abundances of Anders & Grevesse 1989, while George & Fabian assumed abundances of Anders & Ebihara 1982). We have verified the factor of 1.3 using the Monte Carlo code of Życki & Czerny (1994). Initial direction of Fe $K\alpha$ photons is generated with uniform distribution of azimuthal angle but we consider various distributions of the polar emission angle, $\mu_{\text{em}} \equiv \cos\theta_{\text{em}}$. In most cases we assume a limb darkening in electron scattering limit, $I(\mu_{\text{em}}) \propto 1 + 2.06\mu_{\text{em}}$ but in Sections 3.7 and 4 we take into account other angular laws.

For photons hitting the disc we perform also simulation of Compton reflection. Then, we solve equations of motion in the Kerr metric for both the Fe $K\alpha$ and Compton reflected photons emerging from r_d . The detailed analysis of the spectral component formed by the latter, reaching a distant observer, will be presented in our next paper. Here we

take into account effects due to reflected photons which return to the disc giving rise to fluorescence (Section 3.2). Furthermore, in Section 4.4 we take into account the Compton reflected component for computing the equivalent width of the Fe line.

2.2 The models

We study properties of the iron line, in particular effects related to azimuthal motion and returning radiation, for two extreme locations of the primary source, represented by models *A* and *S*, defined below, with the source located close to the symmetry axis and close to disc surface, respectively. In these models, location of the primary source is given by its BL coordinates, r_s and θ_s . We illustrate effects resulting from varying distance of the source by changing r_s at constant θ_s , which seems appropriate for the innermost part of the flow (e.g. numerical simulations typically show conical coroneae or outflows rather than plane parallel structures). We consider also a recently popular variability model with position of the primary source parametrised by $h_s \equiv r_s \cos\theta_s$, defined as model *C* below, in which the polar position of the source covers the whole range of values of θ_s . Specifically, model *C* is equivalent to model *S* for small h_s and to model *A* for high h_s .

2.2.1 Model A

In model *A* we consider a primary source located close to the axis. All model *A* spectra in this paper correspond to $\theta_s = 0.05$ rad. Our model *A* with $V = 0$ is virtually equivalent to models with on-axis source, e.g. Matt et al. (1992), Martocchia & Matt (1996), Petrucci & Henri (1997), Martocchia, Karas & Matt (2000). Our assumption of location being slightly displaced from the axis allows us to study the impact of azimuthal motion in the polar region.

2.2.2 Model S, S_K , S_0

In model *S* we consider a source located close to the disc surface. All model *S* spectra shown in this paper correspond to $\theta_s = 1.5$ rad, i.e. $h_s = 0.07r_s$. We discuss the dependence of model *S* on V , but in Section 4 we focus on a scenario with the primary source rigidly coupled to the underlying disc and corotating with Keplerian velocity, $\Omega_K(r_s)$. This specific case is denoted as model S_K . For $a = 0.998$ we consider only $r_s > r_{\text{ms}}$. All variability effects in this model are studied for varying distance, r_s , and a constant polar angle θ_s .

We also introduce another model, S_0 , for a non-rotating black hole, $a = 0$, but assuming a quasi-Keplerian velocity of accreting matter in the plunging region below r_{ms} : $v^r = 0$ and $v^\phi = 0.5c$ (instead of the usual free fall assumption). Such a velocity field is very similar to the velocity field of an accretion disc around an $a = 0.998$ black hole, in the region $1.25 < r < 6$ (where $v_K(r = 3.5) = 0.5c$; v_K increases from $0.4c$ at $r = 6$ to $0.57c$ at $r \leq 2$). This model can thus serve as a comparison model to study effects specific to space-time around rapidly rotating black hole, which are significant for $r_s < 6$. We emphasise that we do not consider this as a likely scenario, we are not aware of any results supporting such a rotating flow within r_{ms} [although e.g. Agol

& Krolik (2002) argue that distant regions of the flow may be linked through magnetic tension, which presumably could affect motion of the flow in the plunging region]. We consider model S_0 only to separate effects due to gravitational energy shift and bending of trajectories from kinematic effects.

2.2.3 Model C

Following Miniutti & Fabian (2004) we consider a model with a cylindrical-like motion of the primary source, referred to as model C , with the source located at constant projected radial distance $\rho_s \equiv r_s \sin \theta_s$ and changing the height, h_s , above the disc surface. Furthermore, model C assumes that at each h_s the source has the same angular velocity, equal to the Keplerian velocity at ρ_s , $\Omega_K(\rho_s)$. This yields the following velocity of the source rest frame relative to the LNR frame (Bardeen et al. 1972)

$$V = \frac{\sin \theta A}{\Sigma \Delta^{1/2}} (\Omega_K - \omega). \quad (8)$$

All spectra for model C shown in this paper are for $\rho_s = 2$.

Note that equation (8) yields, for constant angular velocity, a peculiar dependence of V on source location. Namely, V increases with increasing h_s at small heights, achieves a maximum value at $h_s \approx \rho_s$ and then decreases. E.g. for $\rho_s = 2$: $V(h_s = 0) = 0.57$, $V(h_s = 2) = 0.69$ and $V(h_s = 20) = 0.55$. These changes of V , with h_s , appear to be crucial for properties of model C . To illustrate impact of kinematic assumptions, we show in Section 3.5 variability in a model with primary source changing h_s at constant ρ_s , as in model C , but with constant angular momentum equal to angular momentum on a Keplerian orbit in the equatorial plane at ρ_s , l_K [yielding $\Omega = (g^{\phi t} - l_K g^{\phi\phi})/(g^{tt} - l_K g^{t\phi})$].

Suebsewong et al. (2006) study effects of changing ρ_s at constant h_s , keeping parametrisation of the source motion introduced by Miniutti & Fabian (2004). Again, we note that for small h_s , which are most relevant for such scenario, the assumed pattern of motion yields velocity field strongly affecting the derived properties. E.g., for $h_s = 0.5$, $V = 0.6 - 0.8$ for $\rho_s \leq 2$, i.e. achieves values much larger than those of a Keplerian motion in the equatorial plane. Furthermore, results of both Miniutti & Fabian (2004) and Suebsewong et al. (2006) for large ρ_s or h_s are strongly affected by the assumed value of $r_{\text{out}} = 100$, see Section 3.5.3.

2.3 Intrinsic luminosity

In all models we assume that the primary emission has a power-law spectrum, with a photon spectral index $\Gamma = 2$, and an exponential cut-off at $E_{\text{cut}} = 150$ keV [this cut-off energy is (marginally) relevant for the fluorescent line only due to effect of returning radiation]. Units for spectra, presented in Section 3, are arbitrary but all have the same normalisation, with intrinsic luminosity, L_0 , yielding the energy flux of primary emission, per unit solid angle in the rest frame of the source, F_E , normalised to unity at 1 keV. Assumption of constant intrinsic luminosity is released in two cases: (i) in model S_K^{PT} which adopts kinematic assumption of model S_K , but assumes intrinsic luminosity changing with r_s according to dissipation rate per unit area in a Keplerian disc (Page & Thorne 1974); (ii) in models \hat{C} , \hat{S}_K and \hat{S}_0 ,

considered in Section 3.5, which adopt assumptions of models C , S_K and S_0 , respectively, but neglect time dilation at primary source, i.e. assume the source intrinsic luminosity $= L_0/g_t$.

We present spectra averaged over azimuthal angle. Although in models defined above the axial symmetry is broken, the orbital periods are much shorter (with one exception, see below) than the timescale, 10 ks, over which variability properties are investigated in the highest quality data. Note that, for high a , azimuthal averaging is justified also for a source with $V = 0$, which rotates with respect to a distant observer with angular velocity ω , comparable to Ω_K at small r , e.g. $\omega \approx 0.2\Omega_K$ at $r = 4.5$.

For a black hole with $M = 10^7 M_\odot$ the orbital period exceeds 10 ks in model S_K with $r_s > 10$. Indeed, narrow, slightly shifted lines observed in some objects with such large masses are considered to arise from localised spots on the disc (e.g. Dovčiak et al. 2004b) in a model equivalent to our S_K with large r_s . Note, however, that this range of parameters is not relevant to effects considered in our paper. In particular, GR effects are weak and effects of black hole rotation are completely negligible for such distances. We analyse variability effects averaged over an orbital period for such large r_s for potential applicability to lower mass systems.

Finally, we ignore time delays between the primary and reprocessed radiation, related to light-travel times between the source and various parts of the disc. For a central source illuminating the ring of radius $R_d (\gg R_g)$, these delay times are between $(1 - \sin \theta_{\text{obs}})R_d/c$ and $(1 + \sin \theta_{\text{obs}})R_d/c$. For $\theta_{\text{obs}} = 30^\circ$, the minimum and maximum delay is $2.5 \times 10^{-6} r_d M/M_\odot$ s and $7.5 \times 10^{-6} r_d M/M_\odot$ s, respectively. Then, for $M = 10^7 M_\odot$ and $r_d > 150$, the delays exceed typical times, ≥ 10 ks, for high quality spectra.

We emphasise that in most cases these delays are not important to variability effects studied here, regardless of the value of M , as the major part of reprocessed radiation originates from $r_d \lesssim 10$ and the fraction of Fe photons coming from $r_d > 100$ is smaller than 1 per cent. Significant irradiation of disc at $r_d > 100$ occurs only for $h_s > 10$ in model C . In this case the delays may affect variability for large M , we discuss this issue further in Section 3.5.3. We choose $r_{\text{out}} = 600$ because for this value properties of neither of our models are affected by neglecting reflection from distances larger than r_{out} . Even in the most extreme case of model C with $h_s = 20$ contribution from $r_d > 600$ would not exceed 1 per cent. However, in other models a smaller value, e.g. $r_{\text{out}} = 100$, could be safely assumed.

3 RESULTS

3.1 Radial emissivity of Fe $K\alpha$ line.

Fig. 1 shows radial illumination profiles, ϵ_{ph} , and corresponding radial emissivities of Fe photons, ϵ_{Fe} , resulting from illumination of the disc surface by a point source. The ϵ_{ph} and ϵ_{Fe} are given in number of photons, per unit time and unit area of the disc, hitting the disc surface and emerging from the disc, respectively, at distance r_d . All radial profiles are averaged over the azimuthal angle, ϕ .

Note that the illuminating flux as well as photon emission rate are equal when expressed both in the BL coordinate frame and in the disc rest frame

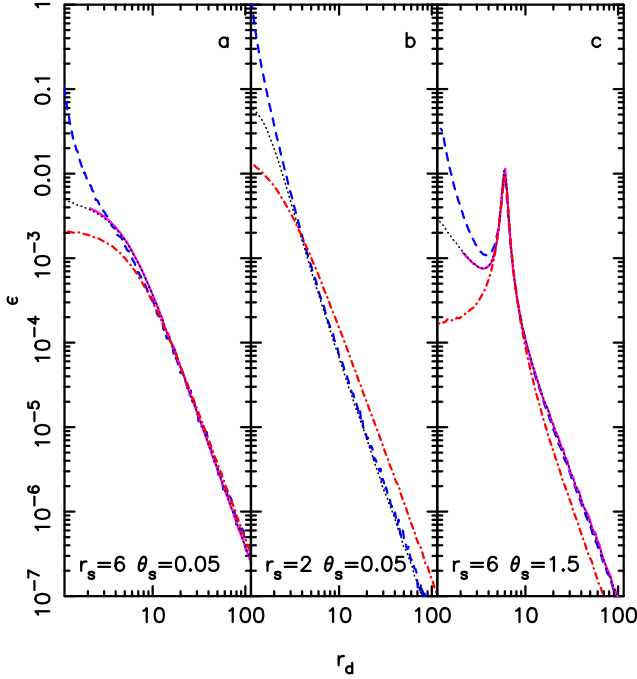


Figure 1. Radial illumination (ϵ_{ph}) and Fe K α emissivity (ϵ_{Fe}) profiles, averaged over azimuthal angle, for a disc illuminated by a point source, with $V = 0$: **(a)** model A with $r_s = 6$; **(b)** model A with $r_s = 2$; **(c)** model S with $r_s = 6$. The dotted (black) and dot-dashed (red) curves show ϵ_{ph} in the Kerr (with $a = 0.998$) and flat space-time, respectively. The solid (magenta) curves in panels (a) and (c), approximately coincident with the dotted curves at $r_d > 2$, show ϵ_{ph} for the Schwarzschild space-time. The dashed (blue) curves show ϵ_{Fe} for the Kerr metric (and photon spectral index $\Gamma = 2$). The illuminating photon flux is normalised by total number of photons emitted from the primary source. The ϵ_{Fe} profiles are normalised to dotted curves at large r_d . Deviations between dot-dashed and dotted curves illustrate impact of GR effects on the radial illumination pattern. Deviations between dotted and dashed curves are primarily due to blueshift of photons in the disc rest frame.

$$\epsilon \equiv \frac{N_{\text{ph}}}{d\hat{t}d\hat{S}} = \frac{N_{\text{ph}}}{dt_d dS_d}, \quad (9)$$

where N_{ph} is the number of photons, $d\hat{t}$ and dt_d is the time interval in BL and disc rest frame, respectively, and $d\hat{S}$ and dS_d is the surface area element in the BL and disc rest frame, respectively. Namely, the following relations $dS_d = \gamma(A/\Delta)^{1/2} r^{-1} d\hat{S}$ (e.g. Petrucci & Henri 1997) and $dt_d = \gamma^{-1} r(\Delta/A)^{1/2} d\hat{t}$ (cf. equation (7); γ is the Lorentz factor corresponding to Kepler velocity, v_K , of disc element with respect to the LNR frame) imply that both GR and special relativistic (SR) effects cancel out. Note also that (Lorentz) transformation between the disc rest frame and the LNR frame (labelled by 'ln' subscript) includes additional time retardation terms, $dS_{\text{ln}} = \gamma^{-1}(1 - \mu v_K/c)^{-1} dS_d$ and $dt_{\text{ln}} = (1 - \mu v_K/c)\gamma dt_d$ (where μ is cosine of the angle, in disc rest frame, between the direction of motion of a surface element and the direction of emitted/incident photon), which again cancel out (Mathews 1982, Laor & Netzer 1990), yielding $dt_{\text{ln}} dS_{\text{ln}} = dt_d dS_d$ (the same conclusion follows trivially from Lorentz invariance of the space-time

volume between the LNR frame and the disc rest frame; Petrucci & Henri 1997).

For clear illustration of effects resulting from light bending, we compare in Fig. 1 the ϵ_{ph} profiles for a black hole accretion disc and a disc in flat space-time, with the same position of the primary source when expressed in BL and spherical coordinates, respectively. The profiles for a static point source in flat space-time are determined by obvious geometrical effects involving the distance from the primary source to disc element and projection of the disc area, yielding

$$\epsilon_{\text{ph}}(r_d) \propto \int_0^{2\pi} [r_d^2 + h_s^2 + \rho_s^2 - 2r_d \rho_s \cos(\phi)]^{-3/2} d\phi, \quad (10)$$

where $\rho_s (= r_s \sin \theta_s)$ is the distance of the source from the symmetry axis, $h_s (= r_s \cos \theta_s)$ is the height of the source above the disc surface and ϕ is an azimuthal angle in the disc plane. For $\rho_s \ll h_s$, Figs. 1(a)(b), the profile is flatter in the central region (at $r_d < h_s$) and steepens to $\epsilon_{\text{ph}} \propto r_d^{-3}$ at $r_d \gg h_s$. For $\rho_s > h_s$, Fig. 1(c), the profile has a steep local maximum at $r_d \approx \rho_s$.

In the black-hole model, light bending enhances illumination of the central region. For a source close to the symmetry axis the deflection of light gives rise to ϵ_{ph} significantly steeper, in the innermost few R_g , than in the flat model. Note, however, that only $r_s \lesssim 2$, Fig. 1(b), leads to steep illumination profile, with $q \gtrsim 3$, where by q we denote index of a power-law approximating locally the radial profiles, i.e. $\epsilon \propto r_d^{-q}$. For a source located close to the disc surface, Fig. 1(c), deflection of photon trajectories increases illumination of the opposite (to the source) side of the disc, enhancing ϵ_{ph} both at $r_d < r_s$ and (moderately) at $r_d > r_s$.

Dashed curves in Fig. 1 show emissivity of Fe K α photons for the model with $a = 0.998$. Within $r_d \lesssim 4$, the ϵ_{Fe} profile is steeper than ϵ_{ph} . This effect is primarily due to the gravitational blueshift of photons hitting the disc surface, which increases the number of photons with energies above the photoelectric threshold. Note, however, that very steep ($q \gtrsim 4$) ϵ_{Fe} occurs only in the part of the disc extending within the ergosphere [the ergosphere is the region contained within the surface given by $r_{\text{erg}} = 1 + (1 - a^2 \cos^2 \theta)^{1/2}$ (≈ 2 for $a = 0.998$ and $\theta = \pi/2$)] where the gravitational blueshift is sufficiently high, e.g., $E_{\text{disc}}/E_s > 4$ at $r_d = 2$ and > 10 around $r_d = 1.2(\approx r_{\text{ms}})$, where E_s is the photon energy in the source rest frame.

3.2 Bending to the equatorial plane

Trajectories of photons emitted from a source located at $r_s > 4$ are bent toward the centre, which effect operates in the same way regardless of the black hole spin value. As a result, identical profiles of ϵ_{ph} (at $r_d > 2$) are achieved for high and low value of a , see Figs. 1(a)(c), in models with $r_s > 4$. For a source located within $r_s < 4$ from a rapidly rotating black hole, an effect unique for the Kerr metric operates, namely the emission is strongly focused along the equatorial plane (Cunningham 1975, Dabrowski et al. 1997). This property of the Kerr space-time leads to significant enhancement of illumination of the disc lying in its equatorial plane, particularly for a source located within the ergosphere. Strength of the bending decreases with increasing

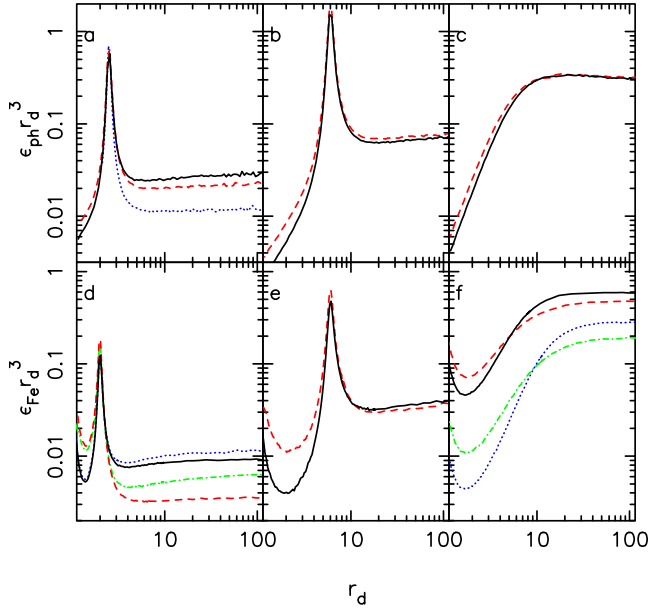


Figure 2. The figure illustrates dependence of ϵ_{ph} (panels a-c) and ϵ_{Fe} (panels d-f) on azimuthal velocity of the primary source. Panel (a) illustrates also bending to equatorial plane in the Kerr metric by comparing ϵ_{ph} for $a = 0$ and $a = 0.998$. Panel (d) shows effect of returning radiation on ϵ_{Fe} for $V = 0$ and $V = 0.5$. All ϵ_{ph} and ϵ_{Fe} , except for dotted (blue) curve in panel (a), are for $a = 0.998$. Panels (a-c) show ϵ_{ph} resulting from direct illumination (i.e. neglecting returning radiation) for a source, with $V = 0.5$ (solid curves, black) and $V = 0$ (dashed curves, red): (a) model S with $r_s = 2.5$; (b) model S with $r_s = 6$; (c) model A with $r_s = 6$. The dotted (blue) curve in panel (a) is for model S with $a = 0$, $V = 0$ and $r_s = 2.5$. (d) Model S with $r_s = 2$. The solid (black) and dashed (red) curves are for $V = 0.5$ and $V = 0$, respectively, and result from direct illumination; the dotted (blue) and dot-dashed (green) curves are for $V = 0.5$ and $V = 0$, respectively, and take into account the returning radiation. (e) Model S with $r_s = 6$. The solid (black) and dashed (red) curves are for $V = 0.5$ and $V = 0$, respectively. (f) The solid (black) and dashed (red) curves are for model A , $r_s = 6$, with $V = 0.5$ and $V = 0$, respectively. The dotted (blue) and dot-dashed (green) curves are for model C , $h_s = 8$, with $V \approx 0.6$ [resulting from equation (8)] and $V = 0$, respectively.

r_s , but for $2 < r_s \lesssim 4$ this effect remains crucial, e.g. a source with $V = 0$ located at $r_s = 2.5$ yields ϵ_{ph} by a factor of 2 higher for $a = 0.998$ than for $a = 0$, see Fig. 2(a). Crucially for the strength of the Fe line observed by low-inclination observers, bending to the equatorial plane enhances irradiation of disc at $r_d > r_s$, while bending toward the centre, which is a dominant effect for higher r_s , enhances irradiation at $r_d < r_s$.

Deflection of photon trajectories toward the equatorial plane affects both the primary emission and radiation reflected from inner parts of the disc (see Cunningham 1976). The former case is crucial for properties of model S as we discuss in Section 3.5. The latter results in redistribution of illuminating flux on the disc surface and in some cases yields significant increase of the Fe line flux, as we show in this section.

Enhancement of Fe $K\alpha$ line by returning radiation was studied by Dabrowski et al. (1997) in a model with a source corotating with the disc, consistent with our model S_K . They

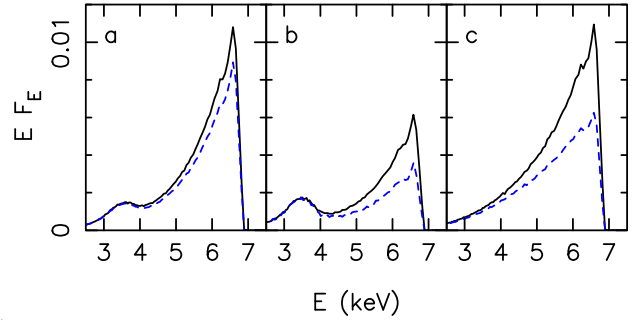


Figure 3. Effect of returning radiation on profiles of Fe $K\alpha$ line for $\mu_{\text{obs}} = 0.85$. The dashed (blue) profiles result from direct illumination only, the solid (black) profiles take into account returning radiation. (a) Model S with $V = 0.5$ and $r_s = 2$. (b) Model S with $V = 0$ and $r_s = 2$. (c) Model A with $V = 0$ and $r_s = 2$.

find that the returning continuum photons increase the flux of the line by no more than 20 per cent. In generic agreement with Dabrowski et al. (1997), we find in model S with $V = 0.5$ (and similarly in model S_K), with small r_s , that returning continuum photons increase ϵ_{Fe} at $r_d > r_s$ by $\gtrsim 10$ per cent, see Fig. 2(d), yielding enhancement of the line by the same order of magnitude, see Fig. 3(a). This property is obvious, as (i) the reflecting albedo around the Fe $K\alpha$ edge is about 10 per cent and (ii) transfer of photons from both the corotating source and the disc under the source, to other regions of the disc, is similar. The overall effect of the returning radiation has a minor impact on model involving primary source corotating with the disc (see also Fig. 7(b) below).

However, we note that a significantly stronger enhancement of the line by returning photons may occur if the source does not corotate with the disc. Equations (3) and (4) yield

$$E_{\text{inf}} = \frac{E_{\text{ln}}}{1 - \omega\lambda}, \quad (11)$$

which implies that the gravitational shift of photon energy between the source, r_s , and the disc, r_d ,

$$\frac{E_{\text{ln}}(r_d)}{E_{\text{ln}}(r_s)} = \frac{1 - \lambda\omega(r_d)}{1 - \lambda\omega(r_s)}. \quad (12)$$

increases with decreasing λ for $r_s > r_d$. Then, the average gravitational blueshift is higher for lower V (implying on average lower λ of emitted photons). Furthermore, for model S with $V = 0$, Doppler blueshift of illuminating photons is high due to velocity gradient between the source and the disc. Combination of the above two effects results in higher blueshift, for smaller V , of photons illuminating disc within the ergosphere and thus in the increase of magnitude of radiation reflected from $r_d < 2$ - most of which returns to the disc, enhancing ϵ_{Fe} more efficiently than for $V = 0.5$. E.g. in model S with $r_s = 2$ and $V = 0$, the resulting enhancement of ϵ_{Fe} [Fig. 2(d)] and of the line flux [Fig. 3(b)] exceeds 50 per cent. Even more significant effect occurs for a source with a very centrally concentrated (and weak beyond a few R_g) direct illumination of the disc, specifically, for a source with $V = 0$ at a small r_s in model A , see Figs. 4(a) and 3(c). E.g. for $r_s = 1.6$, due to contribution of returning radiation, the line flux increases by a factor of ≈ 3 .

Enhancement of the Fe line by returning radiation is

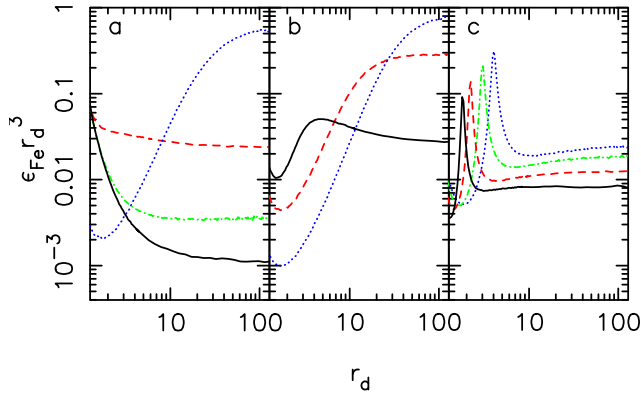


Figure 4. Radial ϵ_{Fe} profiles resulting from direct illumination in our basic models. **(a)** Model A with $V = 0$ and $r_s = 1.6$ (solid curve, black), 3 (dashed curve, red) and 20 (dotted curve, blue). **(b)** Model C with $h_s = 2$ (solid curve, black), 8 (dashed curve, red) and 20 (dotted curve, blue). **(c)** Model S_K with $r_s = 1.8$ (solid curve, black), 2.2 (dashed curve, red), 3 (dot-dashed curve, green) and 4 (dotted curve, blue). The dot-dashed (green) curve in panel (a) takes into account contribution of returning radiation for $r_s = 1.6$.

efficient only for small r_s . For $r_s > 3$, the flux of returning radiation is in general much smaller than the directly illuminating flux. Note also that all effects discussed in this section are unique for high a models. Specifically, we find that for $a = 0$ returning radiation enhances the Fe line flux at most by a few per cent.

3.3 Azimuthal motion

We point out that azimuthal motion of the primary source affects strongly the line flux through combination of GR and SR effects. The relevant SR effects are discussed by Reynolds & Fabian (1997). Doppler shifts and aberration of the primary emission influence both the number and average direction of primary photons above the iron photoelectric threshold in the disc rest frame. On the other hand, azimuthal motion reduces slightly both the illuminating and observed flux due to Lorentz time dilation (by $1/\gamma \approx 0.87$ for $V = 0.5$).

Additional effects occur for a black hole accretion disc, most pronouncedly for small r_s (< 4) and high a . With increasing V , collimation toward direction of motion ($+\phi$ direction) increases fraction of photons bent toward the equatorial plane and thus enhances ϵ_{ph} . For $2 < r_s \lesssim 4$, this effect is moderate, e.g. in model S with $r_s = 2.5$ increase of velocity from $V = 0$ to $V = 0.5$ results in increase of ϵ_{ph} at $r_d > 3$ by 20 per cent, see Fig. 2(a). Much more efficient increase of the fraction of primary photons bent to the disc - with increasing velocity - occurs for $r_s \lesssim 2$. Furthermore, the SR collimation increases the average $p_{(\phi)}$ and therefore the average energy of primary photons increases, see equation (3), yielding additional enhancement of the ionizing flux of photons hitting the disc. Combination of these effects results in a strong enhancement of ϵ_{Fe} by increasing V . E.g., in model S with $r_s = 2$, increase of V from $V = 0$ to $V = 0.5$ results in the increase of ϵ_{Fe} by a factor of 2.5, Fig. 2(d).

Note that the enhanced irradiation of the disc by a source with higher V , discussed above, results only from the

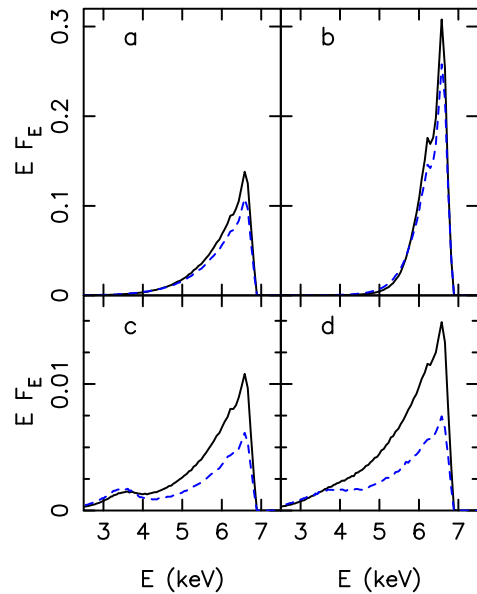


Figure 5. Impact of the primary source azimuthal velocity on the Fe K α line profiles for $\mu_{obs} = 0.85$. Panels (a) and (c) compare profiles for $V = 0.5$ (solid, black) and $V = 0$ (dashed, blue) in model A with $r_s = 6$ (a) and in model C with $r_s = 2$ (c). Panels (b) and (d) are for model C with $h_s = 20$ (b) and $h_s = 0.5$ (d); the solid (black) profiles are for V resulting from equation (8), i.e. $V = 0.55$ (b) and $V = 0.59$ (d); the dashed (blue) profiles are for the same locations of primary source but with $V = 0$. All profiles include contribution of returning radiation.

direct emission from the source. On the other hand, models with smaller V are characterised by stronger contribution of returning radiation, as discussed in Section 3.2. Figs. 5(c)(d) show example profiles of lines for $V = 0$ and $V \approx 0.5$, in models with $r_s \approx 2$.

For $r_s > 4$ changes of the line caused by change of V are more subtle, see Figs. 5(a)(b), and result mostly from the Doppler blueshift. As shown in Figs. 2(b)(c), increase of V approximately does not change ϵ_{ph} at $r_d > r_s$ (assuming that the photon emissivity rate in the source rest frame does not change). Although the SR collimation of primary emission into the direction of motion increases the fraction of photons illuminating the disc at $r_d > r_s$, this increase is balanced by the SR time dilation. On the other hand, increase of V reduces ϵ_{ph} in the central region of the disc, more noticeably for small h_s (compare Fig. 2(b) and Fig. 2(c)), which effect is, however, not important for face-on observers. Then, for high r_s , dependence of ϵ_{Fe} (and hence of the emitted line) on V is mostly due to Doppler shifts. These energy shifts are slightly higher for increasing h_s due to higher, on average, velocity gradient between the source and the disc.

In general, the above GR and SR effects enhance the illuminating flux at the expense of the primary flux observed at low inclinations, which increases sensitivity of variability models (Section 3.5) on assumptions regarding the azimuthal motion. As in Section 3.2, we emphasise that the GR effects discussed in this section are specific for models involving a rapidly rotating black hole.

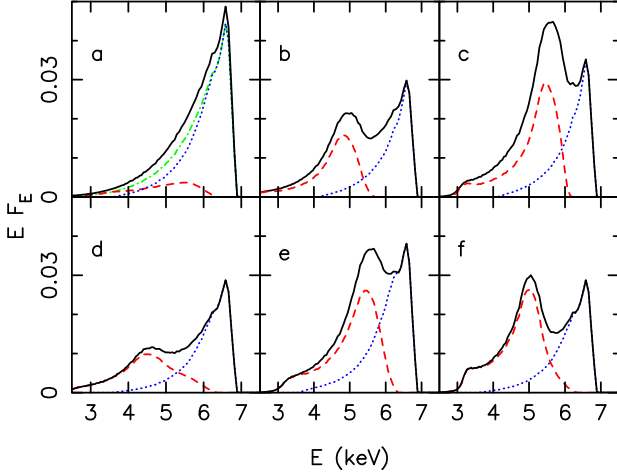


Figure 6. Impact of the space-time metric on the Fe K α line profiles for $\mu_{\text{obs}} = 0.85$. (a) Model A, with $V = 0$ and $r_s = 4$. The solid (black) and dot-dashed (green) curve is for $a = 0.998$ and $a = 0$, respectively. Panels (b–f) are for models S with $V = 0.5$: (b) $r_s = 3$, $a = 0.998$; the dashed (red) curve shows contribution of photons emitted from a narrow ring ($r_d = 3.5 - 4.5$) under the source, the dotted (blue) curve shows contribution of photons emitted from $r_d > 7$; (c) $r_s = 4$, $a = 0.998$; the dashed (red) and dotted (blue) curve shows contribution of photons emitted from $r_d = 4.5 - 5.5$ and $r_d > 7$, respectively; (d) $r_s = 4$, $a = 0$ (free fall within r_{ms}); (e) $r_s = 5$, $a = 0$ (free fall within r_{ms}); (f) Model S_0 with $r_s = 4$. Profiles for $a = 0$ in panels (a,d,e,f) are decomposed into contribution from the region of the disc within r_{ms} (dashed, red) and beyond r_{ms} (dotted, blue).

3.4 The red wing

In this section we focus on the shape of the red wing (i.e. < 6 keV) of the line, which is formed mostly by photons emitted within a few ($\lesssim 6-7$) R_g . We consider effects of space-time metric on the red wing shape and we indicate properties of model S which uniquely allow to investigate effects related to value of a . Applicability of various models to modelling the elongated wing observed in MCG–6–30–15 is discussed in Section 4.1.

Profiles emerging due to combined emission from various r_d have qualitatively similar shapes for low and high a , see Fig. 6(a)]. The smooth low-energy tails of such line profiles indicate that photons forming them come from a region at a few R_g but they do not possess features allowing to constrain more detailed properties of the emitting region, specifically the space-time metric. In particular, change of the angular law, $I(\mu_{\text{em}})$, has at least the same influence on the line shape as a change of the value of a , compare Figs. 6(a) and 16. Then, it has been argued (e.g. Dovčiak, Karas & Yaqoob 2004a) that these time-averaged line profiles do not contain sufficient information to yield unambiguous information about the black hole spin. Such a featureless wing is always produced as a result of illumination by a source close to the axis, i.e. in our model A and similarly in model C (except for very small h_s , see discussion of model S below).

Detection of photons with energies $E_{\text{obs}} < 4$ keV, i.e. redshifted by $E_{\text{obs}}/E_{\text{disc}} < 0.6$, is the key property which could be used to infer a high value of a (for small inclinations). Presence of such photons in the Fe K α line may

distinguish high from low values of a , under the assumption that in the latter case the Fe photons emerge only from $\geq r_{\text{ms}}$. If contribution from within r_{ms} is taken into account, profiles in models with $a = 0$ and $a = 0.998$ extend down to similar energies, see Fig. 6(a). Models of the plunging region (e.g. Young, Ross & Fabian 1998) assess full ionization at $r_d < 5$ for $a = 0$, ruling out contribution from that region. However, they make several simplifying assumptions, most importantly, they base on properties of a test particle motion.

Regardless of these details, escape probability from the region producing photons observed at < 4 keV is small. Therefore, even for a source at a small height on the symmetry axis, the resulting Fe flux below 4 keV is rather weak, see the solid profile in Fig. 6(a), and it may be difficult to deconvolve this emission from continuum components. Generation of a pronounced wing at such energies requires a source located close to the disc surface in the region emitting photons with the most extreme redshifts (see also Section 4.1). We point out that effects of space-time metric can be studied in line profiles emerging in such cases, specifically, for a source located at (i) $r_s \lesssim 4$ and (ii) close to the disc surface ($h_s \leq 0.1r_s$). In such a case, most of fluorescent photons are emitted from a relatively narrow ring, with the width $\Delta r_d \lesssim 1$, under the primary source, see Fig. 4(c). Emission from this ring has a well defined gravitational redshift as well as Doppler shifts. For $\mu_{\text{obs}} = 0.85$, magnitude of the gravitational redshift ($E_{\text{inf}}/E_{\text{LN}} < 0.7$ for $r_d < 4$) exceeds the Doppler blueshift and photons emitted from $r_d \approx r_s$ form a clear feature, indicated by dashed curves in Figs. 6(b,c), with a pronounced blue horn (at 4–5.5 keV, depending on r_s) and a strongly suppressed red horn. Note also that the overall profiles always have a strong blue peak around 6.5 keV, resulting from emission from larger ($\gtrsim 7R_g$) distances. While energy of the latter allows to constrain the inclination angle, the energies and heights of the horns from $r_d \approx r_s$ allow to study effects of space-time metric. Namely, equation (3) implies that the gravitational redshift of photons emitted from $r_d \lesssim 4$ depends on a noticeably; e.g. for $\mu_{\text{obs}} = 0.85$ and $r_d = 4$, photons are redshifted by $E_{\text{inf}}/E_{\text{LN}} = 0.71$ for $a = 0$, while for $a = 0.998$ their redshifts are in the range $E_{\text{inf}}/E_{\text{LN}} = 0.66 - 0.77$ (for $a = 0.998$ the redshift depends on photon initial direction via $p_{(\phi)}$). Then, ≈ 10 per cent difference in energies of the horns (formed at $r_d \approx r_s$) may be expected between low and high a . Furthermore, for photons originating from $r_d \lesssim 4$, the space-time metric affects trajectories, which is reflected in heights of the horns.

Indeed, such differences between model S with $a = 0.998$ and model S_0 , both with $r_s = 4$, are clear in Fig. 6(c,f). Note that these differences result only from GR effects - in both cases the disc under the source has $v_K \simeq 0.5c$. In Fig. 6(d,e) we show spectra for model S with $a = 0$ (and the usual assumption of free fall within r_{ms}). Due to additional Doppler redshift ($v^r < 0$) the redshifted horns have lower energies and are suppressed with respect to the blue peak more significantly than in models S_0 with the same r_s .

3.5 The GR models of spectral variability

Uncorrelated variability between direct continuum and reflection components (including the iron line) revealed in several objects is difficult to understand if we observe the same

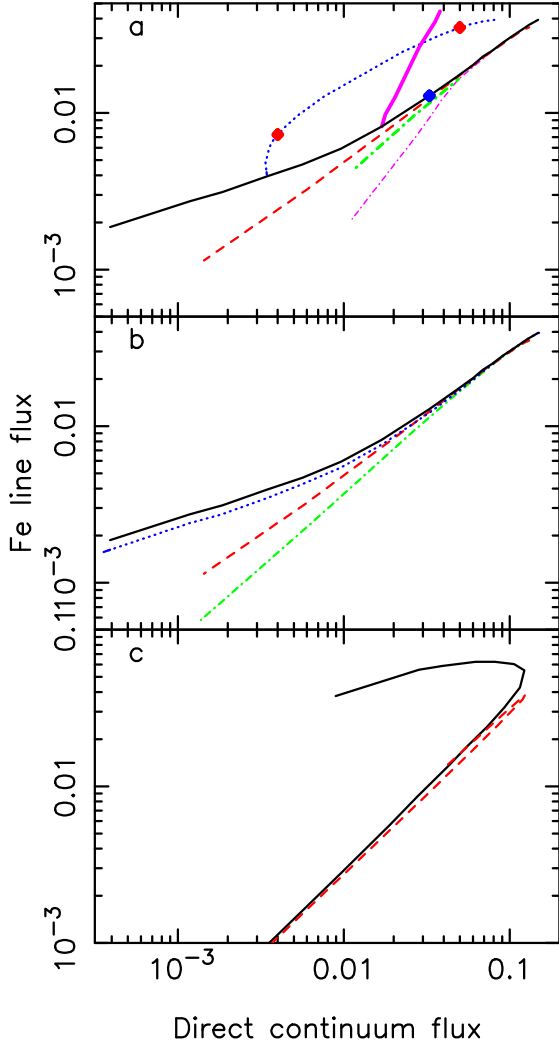


Figure 7. Total flux in the Fe K α line vs the primary emission flux observed at $\mu_{\text{obs}} = 0.85$. All models in panels (a) and (b) assume a constant intrinsic luminosity of the primary source, changes of the observed fluxes result from varying position of the source (in general increasing distance corresponds to increase of the fluxes). (a) The solid (black) curve is for model S_K with $a = 0.998$ and the radial distance between $r_s = 1.5$ and $r_s = 100$; the (blue) diamond is for $r_s = 4$. The dashed (red) curve is for model A with $a = 0.998$, $V = 0$ and $r_s = 1.6$ – 20 . The dotted (blue) curve is for model C with $h_s = 0.07$ – 20 ; the (red) diamonds are for $h_s = 1$ (left) and $h_s = 8$ (right). The heavier dot-dashed (green) curve is for model S_0 and the thinner dot-dashed (magenta) curve is for model S_K with $a = 0$ (and a free fall inside r_{ms}); both models with $a = 0$ are for $r_s = 3$ – 100 and assume $V = 0.5$ at $r_s < 6$. The heavy solid (magenta) curve is for constant $\rho_s = 3$, constant (Keplerian) angular momentum and $h_s = 0.07$ – 20 . All models in panel (a) take into account the returning radiation. (b) The solid (black) and dashed (red) curve is for model S_K and A , respectively, same as in panel (a). The dotted and dot-dashed curves are for the same parameters but with neglected effect of returning radiation. (c) The solid (black) and dashed (red) curve is for model S_K^{PT} (i.e. for intrinsic luminosity changing with r_s according to radial emissivity of a Keplerian disc) with $a = 0.998$ and $a = 0$, respectively. The primary source changes distance between $r_s = 1.5$ (for $a = 0.998$) or 6 (for $a = 0$) and $r_s = 100$ (toward the bottom). Normalisations of curves in (c) are chosen to yield the same maximum values of the direct continuum flux.

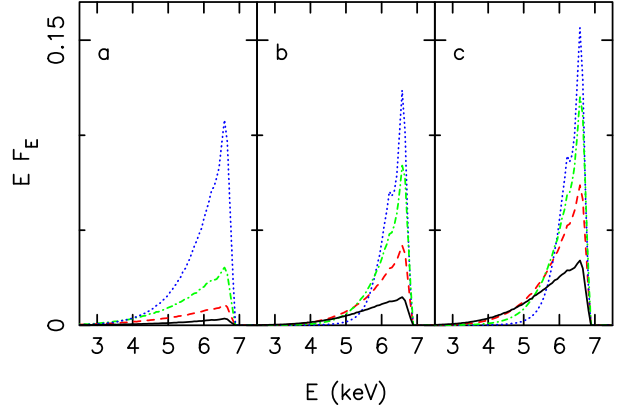


Figure 8. Changes of Fe K α line profile, for $\mu_{\text{obs}} = 0.85$, in models A and C with $a = 0.998$. (a) Model A , $V = 0$, with $r_s = 1.6$ (solid, black), 2 (dashed, red), 3 (dot-dashed, green) and 6 (dotted, blue). (b) and (c) are for model C and \hat{C} , respectively, with $h_s = 2$ (solid, black), 4 (dashed, red), 8 (dot-dashed, green) and 20 (dotted, blue). Profiles in panels (b) and (c) are rescaled by a factor 0.4 .

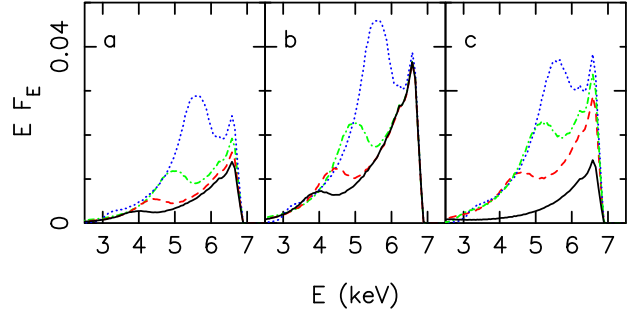


Figure 9. Changes of Fe K α line profile, for $\mu_{\text{obs}} = 0.85$, in model S . Panels (a) and (b) are for model S_K and \hat{S}_K (neglecting the time dilation), respectively, with $a = 0.998$ and $r_s = 2.2$ (solid, black), 2.5 (dashed, red), 3 (dot-dashed, green) and 4 (dotted, blue). Panel (c) is for model \hat{S}_0 with $a = 0$ and $r_s = 3$ (solid, black), 4 (dashed, red), 4.5 (dot-dashed, green) and 5 (dotted, blue).

primary emission that illuminates the disc. As proposed by Miniutti et al. (2003) and Miniutti & Fabian (2004), variability of both the observed continuum and line may be induced by light bending if the primary source is concentrated near the axis of a Kerr black hole. Moreover, they find that variations of both components are not correlated for some range of parameters.

Following Miniutti & Fabian (2004), we compute the observed flux of the primary source vs. that of the Fe line, as the source position is changed, for a source with constant intrinsic luminosity, see Fig. 7(a). Changes of ϵ_{Fe} , related to varying position of the source, in our basic models are shown in Fig. 4; the corresponding changes of line profiles, for model A , C and S_K , are shown in Figs. 8(a), 8(b) and 9(a), respectively.

3.5.1 Model A

In model A, the primary continuum flux changes by two orders of magnitude when the distance of the source varies within $r_s = 1.6 - 20$. However, the line flux varies similarly in this model. At small r_s , directly observed primary flux is significantly reduced while the illuminating flux enhanced by the light bending. The enhanced illumination of the disc is, however, concentrated in the innermost region (at $r_d \lesssim h_s$, see Fig. 1) and the reflected emission is subject to similar bending (due to which most of this emission is lost into black hole) as the primary emission. As a result, the line observed at low inclinations [Fig. 8(a)] roughly follows changes of the continuum. Variations of the line flux are reduced by a factor of ≈ 2 with respect to the continuum flux, primarily due to returning radiation, see Fig. 7(b).

3.5.2 Models S

The most significant reduction of variability of the line flux seems to characterise model S_K , with $a = 0.998$ and $r_s < 4$, where the line flux changes by a factor of 7 while the primary continuum flux changes by two orders of magnitude. On the other hand, in model S_0 (with the same kinematic properties but $a = 0$) both components are linearly correlated, while in model S_K with $a = 0$ (involving free fall within r_{ms}) inward acceleration in the plunging region results in increasing decline of the line flux; see the dot-dashed curves in Fig. 7(a). For $r_s > 6$ model S_K yields the same relation between the line and continuum fluxes (regardless of a) as model A with $V = 0$.

We stress that the reduced variability of the line flux, for small r_s and high a , is directly related to properties of the Kerr metric. Namely, decreasing r_s results in stronger bending to equatorial plane and this in turn gives rise to enhanced illumination of the disc surface at $r_d > 6$, where photons forming the blue peak around 6.5 keV come from, see Fig. 6(b,c). As a result the line profiles, Fig. 9(a), may be decomposed into two components: (i) the redshifted emission from the region under the source, which changes similarly to the primary emission; and (ii) the blue peak with much lower variability.

The distinct properties of the Kerr metric, underlying reduction of the line variability in model S, are clearly illustrated in models neglecting the effect of time dilation at the primary source, i.e. with the source luminosity $= L_0/g_t$, where g_t is given by equation (7); note that the time dilation affects in the same way both the directly observed and illuminating flux, thus increasing magnitude of variability of both the primary and reflected components, but does not change the relative variability of these two components.

The $\epsilon_{Fe}(r)$ profiles in models neglecting time dilation are shown in Fig. 10. In model \hat{S}_K with $a = 0.998$, focusing of primary emission toward the disc yields constant $\epsilon_{Fe}(r)$ in the region where photons forming the blue peak originate. This, in turn, results in identical line profiles at $E > 6$ keV (Fig. 9(b)), while the primary emission flux changes (similarly to the line flux at < 6 keV). A similar neglect of time dilation in model \hat{S}_0 does not result in any range of r_d with similarly constant ϵ_{Fe} , Fig. 10(b); in this case flux in the blue peak is strictly correlated with the primary flux, see Fig. 9(c).

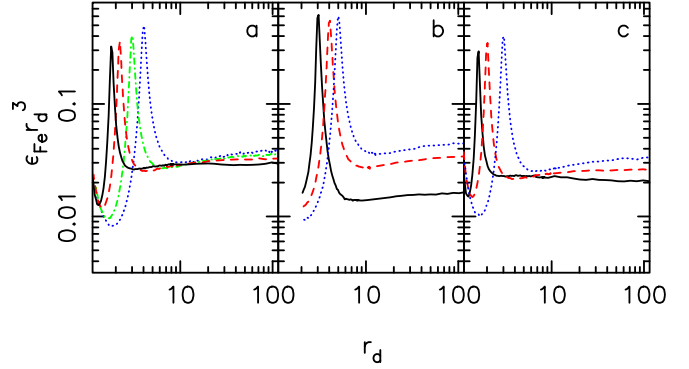


Figure 10. Changes of $\epsilon_{Fe}(r)$ resulting from the change of distance of primary source in models \hat{S} (with neglected time dilation). Panels (a) and (c) show impact of azimuthal velocity pattern, Keplerian vs constant with $V = 0.5$, for $a = 0.998$. Panels (b) and (c) show effect of black hole spin, $a = 0$ vs 0.998 , for constant $V = 0.5$. (a) The solid (black), dashed (red), dot-dashed (green) and dotted (blue) curves are for model \hat{S}_K with $a = 0.998$ and $r_s = 1.8, 2.2, 3$ and 4 . (b) The solid (black), dashed (red) and dotted (blue) curves are for model \hat{S}_0 with $V = 0.5$, and $r_s = 3, 4$ and 5 . (c) The solid (black), dashed (red) and dotted (blue) curves are for model \hat{S} with $a = 0.998$, $V = 0.5$ and $r_s = 1.6, 2$ and 3 .

Note also that V increases with decreasing r_s in model S_K , which seems to be the most likely for a source close to the disc surface, as it may be expected to be rigidly coupled to the accretion disc by magnetic fields. In general, the observed line and continuum fluxes are sensitive to assumed V , see Section 3.3 and discussion of model C below. We emphasise, however, that the increase of V in model S_K is not crucial for reduction of variability of the line. For high a and small r_s , bending to the disc plane is a robust effect, exceeding in magnitude other relevant effects. In particular, approximate constancy of $\epsilon_{Fe}(r)$ around $r_d = 10$ is achieved also for fixed V , see Fig. 10(c).

Our simplified description of generation of X-rays by a point source with constant intrinsic luminosity allows to illustrate various GR and SR effects, as in panels (a) and (b) of Fig. 7. Combination of these effects with more realistic modelling of the X-ray source may result in variety of additional properties. A particularly interesting case of model S_K^{PT} , with intrinsic luminosity proportional to the energy release rate in a Keplerian disc, is shown in Fig. 7(c). Effects due to bending to the equatorial plane are again clear in comparison of models involving $a = 0$ and $a = 0.998$. In the former case, both the line and continuum fluxes increase with decreasing r_s (> 10) due to increase of the dissipation rate, however for $r_s < 10$ the fluxes decrease, due to decrease of both the dissipation rate and photon escape probability, following approximately the same relation between the continuum and line flux as at higher r_s . On the other hand, for $a = 0.998$ the primary emission flux achieves the maximum value around $r_s = 3$ and then decreases by a factor of 3 with the distance decreasing to $r_s = 1.8$, while the Fe flux remains almost constant.

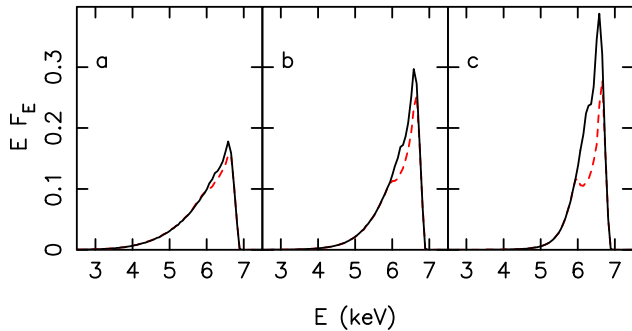


Figure 11. The Fe K α line profiles, for $\mu_{\text{obs}} = 0.85$, in model C with $h_s = 4$ (a), 8 (b) and 20 (c). The solid (black) profiles are for $r_{\text{out}} = 600$ and the dashed (red) are for $r_{\text{out}} = 100$.

3.5.3 Model C

Miniutti et al. (2003) and Miniutti & Fabian (2004) show that with modifications of the model with source close to the axis (see definition of our model C), variability of the line flux is strongly reduced over some range of heights. Specifically, they identify three different regimes in which the iron line is correlated (at small h_s), almost constant (at intermediate h_s) and anti-correlated (at high h_s) with respect to the direct continuum. For $\mu_{\text{obs}} = 0.85$ and $\rho_s = 2$, these regimes correspond approximately to $h_s = 1 - 4$, $h_s = 4 - 13$ and $h_s > 13$, respectively.

The dotted curve in Fig. 7(a) shows the iron line flux [changes of the line profile are shown in Fig. 8(b)] as a function of primary continuum flux for model C . In agreement with Miniutti & Fabian (2004) we find that the primary continuum changes by a factor of 20 for the height varying between $h_s = 1$ and 20. On the other hand, we find different dependence of the line flux on h_s , in particular we do not note a decrease of the line flux at large heights. We suspect that this discrepancy results primarily from different values of the outer radius of the disc, $r_{\text{out}} = 100$ assumed by Miniutti & Fabian (2004) and $r_{\text{out}} = 600$ in this paper. An additional, small difference involves angular law of Fe emission (assumed to be locally isotropic in Miniutti & Fabian 2004), which yields a moderate ($\lesssim 20$ per cent, see Fig. 17) change of quantitative results. On the other hand, value of r_{out} appears to be crucial for qualitative predictions of the model.

The finite extension of the outer radius of the disc results in the presence of a central dip in the line profile, which is not important for the total flux of the line for sufficiently large r_{out} . However, at $h_s > 10$, the solid angle subtended by a disc with $r_{\text{out}} = 100$ is significantly smaller than, e.g. for $r_{\text{out}} = 1000$ (see Matt et al. 1992). Moreover, illumination is shifted to outer regions of the disc in model C due to azimuthal motion. As a result, the line flux is increasingly underestimated with increasing h_s , e.g. by over 30 per cent for $h_s = 20$, in the model with $r_{\text{out}} = 100$, see Fig. 11. We conclude that for face-on observer the anti-correlation is an artificial effect which does not occur if sufficiently large r_{out} is taken into account. On the other hand, we find a real anti-correlation for higher inclinations, see below.

Obviously, illumination of distant regions, and hence the choice of specific value of r_{out} , becomes more important

for increasing h_s . Our aim is to study effects related to GR or SR rather than simple geometric effects related to the change of the solid angle. Therefore, we assume $r_{\text{out}} = 600$, for which reflection from $r_d > r_{\text{out}}$ is negligible (for $h_s \leq 20$), in our computations. Clearly, such a value is necessary for applications of the model to stellar-mass black hole systems (cf. Miniutti, Fabian & Miller 2004). For large black hole masses, $M > 10^7 M_\odot$, part of reflection from distant regions of the disc would be subject to significant delays, owing to light travel-time effects, see Section 2. In such cases, variations of the reprocessed radiation should be somewhat reduced due to mixing of radiation responding to primary emission from various positions of the source. On the other hand, for large h_s , the Fe flux is close to constant even without the mixing effect. A more interesting effect, related to light-travel time in model C , for high values of M , would involve response of the line profile to changes of the source position. In particular, rapid increase of h_s should result in such changes of the line profile as those predicted by Stella (1990). For black holes with lower masses, $M \lesssim 10^7 M_\odot$, impact of time delays on variability properties depends on the range of heights and the time-scale over which the variability is analysed. Note, e.g., that for $M = 6 \times 10^6 M_\odot$ (which is within the range of masses allowed in MCG-6-30-15 by optical measurements, see Section 4), the mixing effect could not be neglected in applications of model C with $h_s \geq 10$.

For $r_{\text{out}} = 600$, taking into account the whole range of heights ($\leq 20 R_g$), we find the following relation between the line and continuum in model C . At $h_s < 1$ the line varies by a factor of 2 while the primary continuum is almost constant. For $h_s = 1 - 8$, variations of the line are reduced by a factor of 2 with respect to the continuum. For $h_s > 8$, the line flux is close to constant. In the last case, majority of Fe photons come from the region of disc where light bending and beaming effects are small and changes of line flux result from varying time dilation at the primary source. Neglecting the time dilation we find that the line flux is constant while the primary flux increases by 50 per cent with increase of height from $h_s = 8$ to $h_s = 20$. Note, however, that although the total line flux does not change, the line profiles change significantly with h_s [see Fig. 8(c)] - in general, flux at 5.8 keV remains approximately constant but the wing below this energy weakens while the blue peak strengthens with the increase of h_s [note the change of the distance where most of Fe photons come from in Fig. 4(b)].

We emphasise that the above behaviour is not a generic prediction, resulting from light bending, for a model involving a source with changing h_s . It is strongly related to specific kinematic assumptions underlying model C , see Section 2.2.3. Apart from impact on the line flux, discussed in Section 3.3, changes of V reduce variability of the primary continuum at small heights (where weaker light bending is balanced by stronger SR beaming with increasing h_s) and enhance its variability at $h_s > 2$. Assuming another pattern of motion, we obtain different relations between the spectral components. E.g., for a source changing h_s at constant ρ_s , but with constant angular momentum equal to angular momentum on a Keplerian orbit in the equatorial plane at ρ_s , V increases monotonically with h_s . In this case, the magnitude of the line flux variability is higher than that of the continuum at all h_s , see the heavy solid curve in Fig. 7(a). On the other hand, setting $V = 0$ in model C we find, for

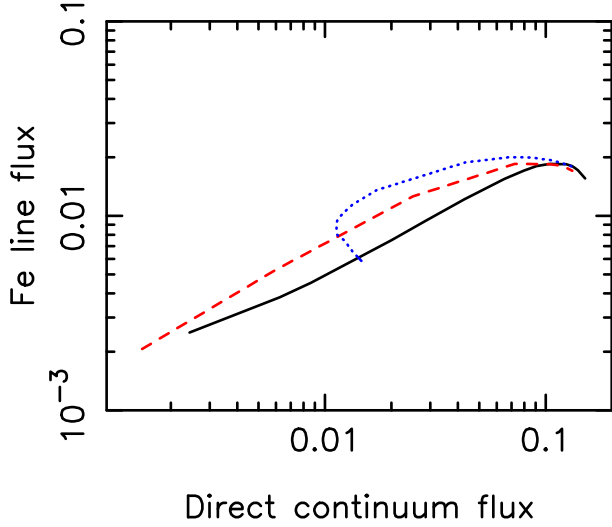


Figure 12. Same as Fig. 7(a) but for an observer inclination $\mu_{\text{obs}} = 0.45$. Solid (black) curve is for model S_K , dotted (blue) for model C , dashed (red) for model A . All models assume $a = 0.998$.

$h_s > 1$, the same relation between the line and primary flux as in model A , i.e. shown by dashed curve in Fig. 7(a).

3.5.4 Summary of variability models

In summary, increased illumination of the innermost disc, within a few R_g , resulting from deflection of light *toward the centre*, is not sufficient to yield reduced variability of reflection component for small inclination angles. The major constraint results from the fact that reflection from this innermost region is not observed at small inclinations. Then, reduction of observed variability requires enhanced illumination of disc beyond a few R_g , which can be achieved in the Kerr metric for small r_s as a result of bending *toward the equatorial plane*. Interestingly, the same mechanism reduces variations of the line for a source at small heights at the axis, through the effect of returning radiation, as this radiation illuminates the disc at distances larger than the source height. Alternatively, a more extended illumination may result from the SR beaming and then the reduced variability can be achieved for appropriate pattern of motion, e.g. for V decreasing with increasing h_s .

On the other hand, the above constraint does not apply to systems with higher inclinations ($\cos \theta_{\text{obs}} < 0.6$) and for such systems the line flux varies with much smaller amplitude than the continuum flux in all models, see Fig. 12. Moreover, anticorrelation between the line and continuum fluxes observed at such θ_{obs} is a generic property of all models at large r_s or h_s . The decrease of the line flux, with increasing r_s , is a purely SR effect, resulting from (i) angular distributions of the line flux, $F(\mu_{\text{em}})$, in the disc rest frame, which declines with decreasing μ_{em} ; (ii) increase of the distance, r_d , where most Fe photons come from with increasing r_s ; and (iii) decrease of the orbital velocity of disc, with increasing r_d , and thus less efficient beaming to high θ_{obs} .

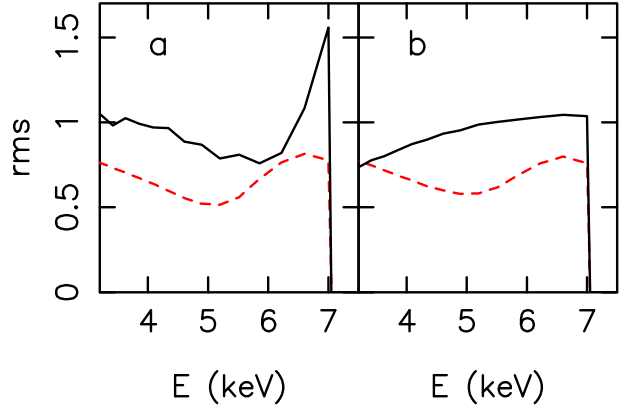


Figure 13. The rms spectra for Fe $K\alpha$ line observed at $\mu_{\text{obs}} = 0.85$. (a) Solid (black) curve is for model S_K with the radial distance changing between $r_s = 1.5$ and $r_s = 100$. Dashed (red) curve is for model C with $h_s = 0.07$ –20. (b) Solid (black) and dashed (red) curve is for model A with $V = 0$ and $h_s = 1.6$ –3 and $h_s = 1.6$ –20, respectively. All models assume $a = 0.998$.

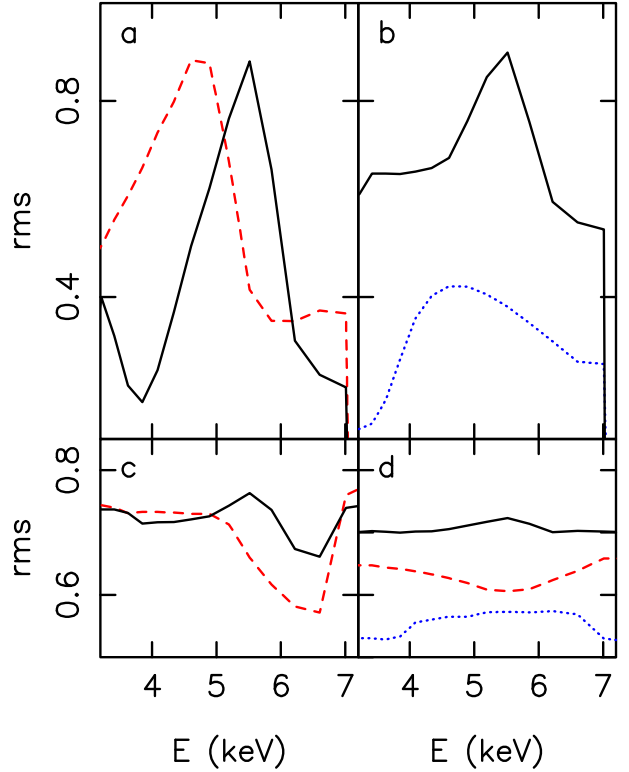


Figure 14. The rms spectra for Fe $K\alpha$ line (top panels) and superposition of Fe line and primary continuum (bottom panels) observed at $\mu_{\text{obs}} = 0.85$. (a,c) The dashed (red) and solid (black) curves are for model S_K , $a = 0.998$, with $r_s = 1.5$ –3 and $r_s = 2.2$ –4, respectively. (b,d) The dotted (blue) curves are for model C with $a = 0.998$ and $h_s = 0.07$ –1. The solid (black) curves are for model S with $a = 0$ and $r_s = 3$ –5. The dashed (red) curve in panel (d) is for model C with $h_s = 0.07$ –20 (i.e. the same parameters as for the dashed curve in Fig. 13(a)). Some spectra in panels (c) and (d) are shifted vertically for clarity.

3.6 The fractional variability

We point out that model S with high a is uniquely capable to explain suppressed variability around 6.5 keV in energy-dependent patterns of spectral variability. We focus here on effects related to changes of the Fe line profile. A more detailed analysis of spectral variability, including the Compton reflection component, will be presented in our next paper.

The fractional variability of observed spectra, as a function of energy, is quantitatively characterised by the root mean square (rms) variability function. In models relating variability to change of position of the primary source, we determine the rms spectra according to the following definition

$$\text{rms}(E) = \frac{1}{\langle f(E) \rangle} \sqrt{\sum_{i=1}^N \frac{[f_i(E) - \langle f(E) \rangle]^2}{N-1}}, \quad (13)$$

where the summation is performed over N positions of the primary source, $f_i(E)$ is the photon flux in the energy band, E , corresponding to i -th position of the source and $\langle f(E) \rangle$ is the average photon flux in this band for all N positions.

In Figs. 13 and 14(a,b) we show the rms spectra for the line and in Figs. 14(c,d) for superposition of the line and the primary power-law. Taking into account the full ranges of source positions considered in our basic models - i.e. radial distances $r_s = 1.5-100$ and $r_s = 1.6-20$ in models S and A , respectively, and the height $h_s = 0.07-20$ in model C - we find that the rms spectra for the line increase toward low energies below 5 keV, see Fig. 13, which effect is related to varying strength and extent of the red wing of the line. However, the line flux at < 5 keV is typically much lower than the primary continuum flux, therefore these variations of the red wing do not produce noticeable excesses in the rms spectra of the line plus power-law. On the other hand, both model A and C are characterised by reduced variability of the line flux around 5.5 keV (see Fig. 8(b,c)) which gives rise to declines in the rms spectra both for the line (Fig. 13) and for the line + power-law (dashed curve in Fig. 14(d)). In turn, in model S_K at $r_s > 10$, the line is formed in majority by photons from $r_d \approx r_s$ and the energy of the blue peak changes with r_s , giving rise to strong increase of rms spectrum at $E > 6$ keV, see Fig. 13(a).

In most models, even these predicting the reduced variability of the total line flux, a decline around 6.5 keV does not occur in the rms spectrum. We notice such suppression only in model S_K (and similarly S_K^{PT}) with $a = 0.998$ and $r_s < 4$, where bending to the disc plane yields strongly reduced variability of the blue peak, see discussion in Section 3.5.2. The detailed shape of resulting signal in the rms spectrum depends on the assumed range of r_s , see Fig. 14(a,c). The range of distances extending deeper into the ergosphere corresponds to stronger suppression around 6.5 keV. For $r_s = 2-4$, decline above 6 keV is less pronounced, on the other hand, a strongly variable and relatively strong red wing of the line gives rise to an excess variability around 5.5 keV, see the solid curves in Fig. 14(a,c).

Direct relation of these effects with properties of the Kerr metric is again clearly illustrated by comparing models S_0 and S_K with $a = 0.998$. The rms spectra for model S_0 with a (rather unphysical) assumption of the primary source

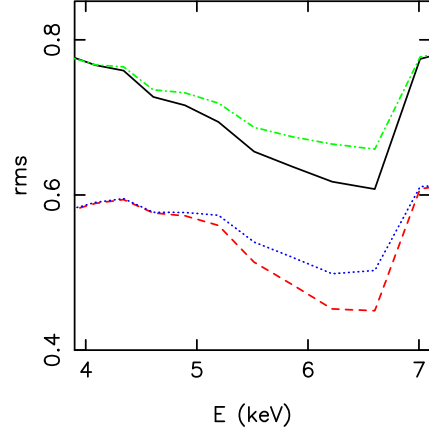


Figure 15. The rms spectra for the superposition of Fe line and primary continuum observed at $\mu_{\text{obs}} = 0.85$, in model S_K^{PT} . The upper and lower pair of curves is for $r_s = 1.7-2.2$ and $r_s = 1.8-3$, respectively. The solid (black) and dashed (red) curves are for $I(\mu_{\text{em}}) \propto 1 + 2.06\mu_{\text{em}}$. The dot-dashed (green) and dotted (blue) curves are for $I(\mu_{\text{em}}) \propto \log(1 + 1/\mu_{\text{em}})$.

changing the radial distance at $r_s < 6$ are shown by the solid curves in Figs. 14(b,d). For $a = 0$, variable red wing gives rise to excess at 5.5 keV, however, the blue peak changes similarly to the primary continuum and the rms spectrum is flat above 6 keV.

We did not find significant differences between predictions of models S_K and S_K^{PT} , see Fig. 15. On the other hand, the quantitative properties are slightly dependent on the angular emissivity law, see next section.

Finally, note that source located close to the disc surface (as required to model a pronounced red wing, see Section 4), but changing the height rather than the radial distance, gives rise to spectral variability significantly different than model S_K . In particular, in model C with small h_s , the line varies much more significantly than the primary emission [see dotted curve in Fig. 7(a)] yielding an extended (over $\Delta E \approx 3$ keV) excess in the rms spectrum, see dotted curves in Fig. 14(b,d). In model A with small r_s (see Figs. 8(a) and 13(b)) the most significant changes of the line occur close to the blue peak.

3.7 Limb darkening

As noted by Beckwith & Done (2004), for a fixed radial emissivity change of the limb darkening may strongly influence the line profile. Therefore, we have checked our results for various angular laws considered in literature.

The limb darkening in the form $I(\mu_{\text{em}}) \propto 1 + 2.06\mu_{\text{em}}$, assumed in most of our calculations, approximates emission from a disc with ionised atmosphere. The same angular distribution is assumed in the LAOR model (see Laor 1991), which is often applied in spectral analysis. Emission from a uniform, not ionised slab is approximated by $I(\mu_{\text{em}}) \propto \log(1 + 1/\mu_{\text{em}})$, Ghisellini, Haardt & Matt (1994). Emission from an optically thin material has $I(\mu_{\text{em}}) \propto 1/\mu_{\text{em}}$. Finally, a locally isotropic emission, $I(\mu_{\text{em}}) = I_0$, is sometimes considered for simplicity.

Fig. 16 shows line profiles for various angular emission

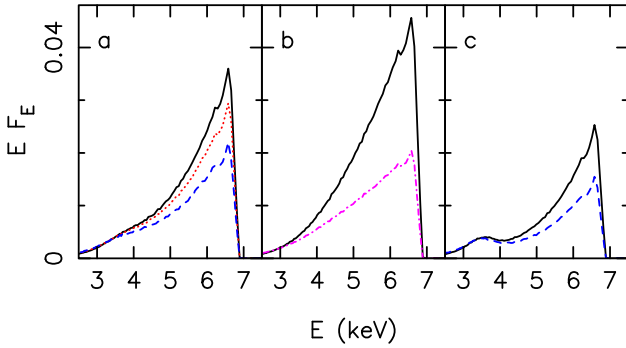


Figure 16. Fe K α line profiles observed at $\mu_{\text{obs}} = 0.85$ for various angular laws. In all panels the solid (black) profiles are for limb darkening in electron scattering limit, $I(\mu_{\text{em}}) \propto 1 + 2.06\mu_{\text{em}}$. (a) Model C with $h_s = 0.4$. The dotted (red) curve is for locally isotropic emission, $I(\mu_{\text{em}}) = I_0$; the dashed (blue) curve is for $I(\mu_{\text{em}}) \propto \log(1 + 1/\mu_{\text{em}})$. (b) Model C with $h_s = 1$. The dot-dashed (magenta) profile is for optically thin emission, $I(\mu_{\text{em}}) \propto 1/\mu_{\text{em}}$. (c) Model S with $r_s = 2$ and $V = 0.5$; the dashed (blue) curve is for $I(\mu_{\text{em}}) \propto \log(1 + 1/\mu_{\text{em}})$.

laws. Note that change of the angular law results, in some cases, in a significant change of height of the blue peak, while the lowest energy ($\lesssim 3.5$ keV) part is roughly unaffected. Then, the slope of the red wing - connecting the low energy part with the blue peak - changes, following the change of the height of the latter. The following effects result in such properties of the line.

For $\mu_{\text{obs}} = 0.85$, the change of the angular law turns out to be unimportant for the magnitude of contribution of photons emitted from the disc within the ergosphere (forming the observed line at $E_{\text{inf}} \lesssim 3.5$ keV). In this part of the disc, only photons emitted into a narrow range of initial directions, with intermediate values of $\mu_{\text{em}} = 0.4 - 0.6$, are observed at $\mu_{\text{obs}} = 0.85$. Then, flux emitted in these directions remains roughly unaffected by the change of angular law, under the condition that total energy of fluorescent photons emitted from unit area of the disc remains constant.

On the other hand, the blue peak is mostly due to emission from outer regions, where light bending is not crucial. Then, changes in the height of the peak simply correspond to change of the flux emitted to $\mu_{\text{em}} \approx \mu_{\text{obs}}$, again under the condition that the total emitted energy remains constant. E.g., $I(\mu_{\text{em}}) \propto 1 + 2.06\mu_{\text{em}}$ yields $F(\mu_{\text{em}} = 0.85)$ higher by a factor of ≈ 2 , 1.7 and 1.2 than $I(\mu_{\text{em}}) \propto 1/\mu_{\text{em}}$, $I(\mu_{\text{em}}) \propto \log(1 + 1/\mu_{\text{em}})$ and $I(\mu_{\text{em}}) = I_0$, respectively. These factors are in a rough agreement with differences in the heights of the blue peaks in Fig. 16.

In conclusion, we confirm that change of the angular law results in the change of the line profile, mostly in the strength of the blue peak. However, we find that these (systematic) changes of the line do not affect the main conclusions of this paper (assuming that the same angular law characterises emission from the whole disc surface). Specifically, the qualitative properties of variability of the total flux of the line as well as the rms spectra, are negligibly affected by the choice of a particular law. Figs. 15 and 17 (in comparison with Fig. 7) illustrate changes of such properties corresponding to the change of $I(\mu)$ from limb darkened to limb brightened. A slightly weaker signal in the rms spec-

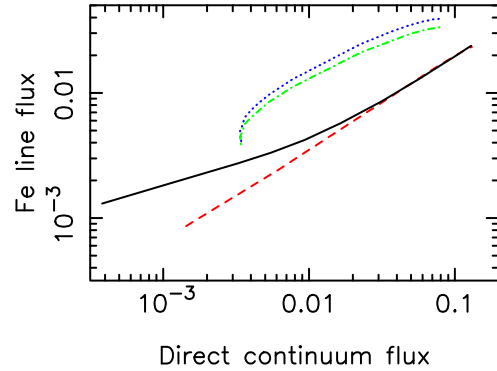


Figure 17. Total flux in the Fe K α line vs the primary emission flux observed at $\mu_{\text{obs}} = 0.85$. The solid (black) and dashed (red) curve is for model S_K and A , respectively, with $a = 0.998$ and constant intrinsic luminosity, same as in Fig. 7(a), but with $I(\mu_{\text{em}}) \propto \log(1 + 1/\mu_{\text{em}})$. The dotted (blue) and dot-dashed (green) curve is for model C with $I(\mu_{\text{em}}) \propto 1 + 2.06\mu_{\text{em}}$ (same as in Fig. 7(a)) and $I(\mu_{\text{em}}) = I_0$, respectively.

trum, for the latter, appears to be the most significant effect resulting from such a change of $I(\mu)$. Note also that changes of the line profile, at $E < 5$ keV, resulting from the change of the angular law are much smaller than changes resulting from significant change of h_s or r_s , compare Figs. 8 and 16, making our conclusions on modelling the extended red wing in the next section independent of angular emission law. Only assumption of $I(\mu_{\text{em}}) \propto 1/\mu_{\text{em}}$ (Fig. 16(b)) could affect our conclusions more significantly, however, such an (optically thin) emission from an accretion disc seems very unlikely.

4 MCG-6-30-15

The profile of broad Fe line in the X-ray spectrum of Seyfert 1 galaxy MCG-6-30-15, first clearly resolved by *ASCA* (Tanaka et al. 1995), is consistent with that predicted from an accretion disc inclined at 30° . In part of the *ASCA* observation, when the 2–10 keV flux was 2 times lower than average, $F_{2-10} = 4 \times 10^{-11}$ erg/s/cm², for the whole observation, the line extended below 4 keV (Iwasawa et al. 1996; that low flux state was defined as the deep minimum). Profiles of the Fe line, extending below 4 keV, were revealed also in two *XMM-Newton* observations (Wilms et al. 2001; Fabian et al. 2002).

During the first *XMM-Newton* observation, in 2000, the average flux, $F_{2-10} = 2.4 \times 10^{-11}$ erg/s/cm², was close to that of the deep minimum. Then, Wilms et al. (2001) and Reynolds et al. (2004) argued that this observation caught the source in its deep minimum state. However, the source was highly variable, changing the flux between $F_{2-10} = 1.5$ and 4.8×10^{-11} erg/s/cm², i.e. below the deep minimum and above the typical flux levels from that source, respectively. During the second, longer observation with *XMM-Newton*, in 2001, with the average $F_{2-10} = 4.1 \times 10^{-11}$ erg/s/cm², the flux again varied, by a factor of 5, between values lower than that of the deep minimum and higher than the typical average value. Using the *RXTE* observations Vaughan & Fabian (2004; see their figure 1 and related discussion) argue

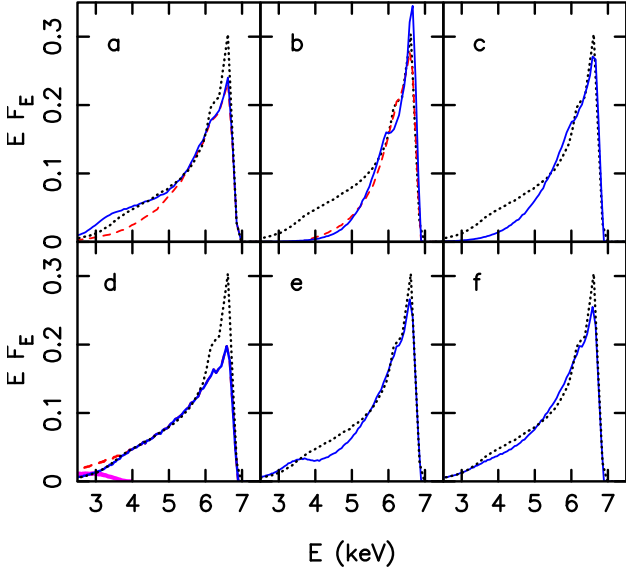


Figure 18. In all panels the dotted (black) curve shows profile of the Fe line derived with parameters given in Fabian et al. (2002), see text. **(a)** The solid (blue) curve is for parameters of the best fit in Vaughan & Fabian (2004), i.e. $q_{\text{in}} = 6.9$, $q_{\text{out}} = 3$, $r_{\text{br}} = 3.4$, $r_{\text{in}} = 1.8$. The dashed (red) curve is for a model with $q = 3$, $r_{\text{in}} = 1.2$ and $a = 0.998$. The solid (blue) curves in panels **(b)** and **(c)** are for model *C* with $h_s = 8$ and 4, respectively, $r_{\text{out}} = 100$ and $I(\mu_{\text{em}}) = I_0$ (as in Miniutti et al. 2003). The dashed (red) curve in **(b)** is for model *A* with $a = 0$, $V = 0$, $r_s = 3$ and $r_{\text{in}} = 6$ ($= r_{\text{ms}}$). The dashed (red) curve in panel **(d)** is for model *A* with $r_s = 1.6$, $a = 0.998$ and $V = 0$. Contribution to this profile from the region of the disc within and beyond $r_d = 2$ is shown by the heavy solid (magenta) and the thinner solid (blue) curve, respectively. **(e)** The solid (blue) curve is for model *S_K* with $r_s = 2$. **(f)** The solid (blue) curve is for model *C* with $h_s = 0.4$. All profiles, except for solid in panels **(b)** and **(c)**, correspond to $I(\mu_{\text{em}}) \propto 1 + 2.06\mu_{\text{em}}$.

that in both cases the source was observed in its typical state.

We focus below on the second *XMM-Newton* observation. A phenomenological model with a broken power-law radial emissivity (see below) gives an excellent fit to the data, with $\chi^2_\nu < 0.9$ (Fabian et al. 2002), therefore, we presume that this model reproduces properties of the emitting region with high precision and we take parameters of the best fit as basic for our discussion.

The most tightly constrained value of the black hole mass in MCG–6–30–15, from X-ray variability, is $\sim 3 \times 10^6 M_\odot$ (in agreement with optical measurements yielding values between 3 and $6 \times 10^6 M_\odot$; McHardy et al. 2005).

4.1 Time-averaged profile

As noted in Section 3.4, detection of photons with energies < 4 keV is considered as the evidence of rapid rotation of a black hole. The best studied example of a relativistic Fe line - with elongated wing formed by such strongly redshifted photons - comes from *XMM-Newton* observation of MCG–6–30–15 (Fabian et al. 2002). This is best fitted with a steep ($q_{\text{in}} = 4.8$) emissivity inside $r_{\text{br}} = 6.5$ and a flatter ($q_{\text{out}} = 2.5$) profile beyond that, and with the inner radius of emitting region $r_{\text{in}} = 2$; the fit was obtained with the LAOR

model (in the X-ray data fitting code XSPEC), which assumes $r_{\text{out}} = 400$ and $I(\mu_{\text{em}}) \propto 1 + 2.06\mu_{\text{em}}$, see Laor (1991). The dotted profiles in all panels of Fig. 18 correspond to those best fitting parameters.

We note that there is a degeneracy between q_{in} and r_{br} , in general higher q_{in} allows for lower r_{br} . Vaughan & Fabian (2004) fit the same *XMM* observation (with the data set extended by including the EPIC pn data) with $r_{\text{br}} = 3.4$ and $q_{\text{in}} = 6.9$, the solid curve in Fig. 18(a). Nevertheless, both sets of parameters require the line flux at 4 keV to be two times larger than in a model assuming a single power-law radial emissivity with $q = 3$ (see Fig. 18(a); the three curves are normalised to yield the same flux in 5–6 keV range). In summary, the data seem to require a steep emissivity in the innermost region to explain strength of the red wing. At larger distances the emissivity has to flatten to produce a rather strong blue peak.

Such steep, broken power-law emissivity profiles can be produced in models with a source positioned close to the symmetry axis (Fig. 1(a,b); see also Martocchia, Karas & Matt 2000), and indeed these models were invoked to explain the broad line profile in MCG–6–30–15 (e.g. Miniutti et al. 2003). We note that in these models the source height has to be rather small if the steep emissivity is to extend beyond the ergosphere (see also Martocchia, Matt & Karas 2002). In particular, we find that in model *C* the steep $\epsilon_{\text{Fe}}(r)$ profile, with $q > 4$, is produced only in the ergosphere, $r_d < 2$, if $h_s > 1$ (Fig. 4(b)). However, photons emitted from within $r_d = 2$ cannot produce the extended red wing observed in MCG–6–30–15, since they are redshifted by $1/g = 2$ –3 (for inclination $\theta_{\text{obs}} = 30^\circ$), and so they are registered at $E < 3.5$ keV (their contribution is shown in Fig 18(d)). Fe lines resulting from $h_s > 1$ do have profiles skewed towards low energies, however they do not possess elongated red wings with approximately constant slope between 3.5 and 5.5 keV, as observed in MCG–6–30–15. For example, for $h_s = 3$ –8, as required by the variability model of Miniutti et al. (2003), the profile is much less pronounced than that corresponding to parameters of the best fit from Fabian et al. (2002) (Fig 18(b,c)); compare with fig. 5 in Miniutti et al. 2003). We find that to fit the profile observed in MCG–6–30–15 model *C* requires the source height $h_s < 1$, see Fig. 18(f).

Similar constraints are obtained in model *A*. Here, in order to produce steep emissivity ($q > 4$) at $r_d > r_{\text{erg}}$, the source must be located at $r_s \lesssim 4$. Explaining the red wing in MCG–6–30–15 requires $r_s \lesssim 2$, with the best agreement achieved for $r_s = 1.6$, Fig. 18(d). This overproduces somewhat the flux below 3.5 keV, if $r_{\text{in}} < 2$ (hence it requires $r_{\text{in}} \simeq 2$, in agreement with Fabian et al. 2002).

Miniutti et al. (2003) claim that their model fits the data for $h_s = 3$ –8. We note that for $h_s > 3$ the flux below 5 keV is actually weaker than for the model with a single power-law with $q = 3$, compare the dashed curve in Fig. 18(a) and the solid curve in Fig. 18(c). Moreover, for $h_s = 8$, the line profile is fully consistent with the one produced by emission only from $r_d > 6$ in a model with $a = 0$, see Fig. 18(b). Then, the fits in Miniutti et al. (2003) appear to contradict results of, e.g., Fabian et al. (2002) who find that strong emission from $r_d < 6$ is required. We suspect that this discrepancy results from modelling of the continuum emission. The simultaneous observation with *Beppo-SAX*, taken into account by Fabian et al. (2002), allows to con-

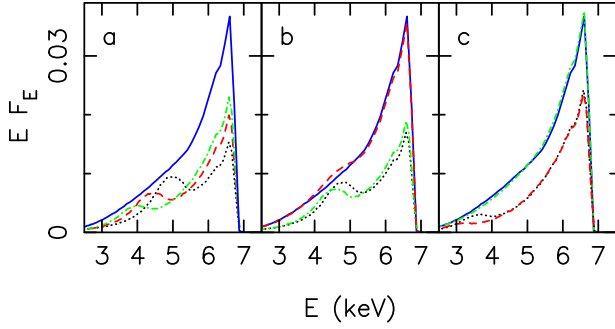


Figure 19. The figure illustrates formation of a profile for superposition of primary X-ray sources in model S_K^{PT} with $I(\mu_{\text{em}}) \propto 1 + 2.06\mu_{\text{em}}$. The profiles for superpositions are rescaled for clarity. The solid (blue) curve in all panels shows the superposition profile for $r_s = 1.8, 2, 2.2, 2.5$ and 3 (D_1). (a) The dotted (black), red (dashed) and dot-dashed (green) curve show individual profiles for $r_s = 3, 2.5$ and 2.2 . (b) The dashed (red) curve shows the superposition profile for $r_s = 1.8, 2, 2.2, 2.4, 2.6, 2.8$ and 3 (D_2). The dot-dashed (green) and dotted (black) curve show individual profiles for $r_s = 2.6$ and 2.8 . (c) The dot-dashed (green) curve shows the superposition profile for sources with $r_s = 1.5, 1.7, 1.8, 2, 2.2, 2.5$ and 3 . The dashed (red) and dotted (black) profiles are for $r_s = 1.8$ and 2 , respectively.

strain the underlying power-law continuum and the Compton reflected component. On the other hand, Miniutti et al. (2003) use only data in 3–10 keV range, which poorly constrains the continuum. Moreover, the fitted value of Γ is not given in their paper so it is not clear if it is consistent with data in broader energy range. Presumably, softer power-law emission may compensate the red wing. We stress, however, that if the model of Miniutti et al. (2003) with, e.g., $h_s = 8$, could fit the data in the broader energy range, it would have an essential implication, namely, rotation of the black hole in MCG–6–30–15 would not be required by the time-averaged profile from the *XMM-Newton* observation.

In general, enhanced illumination of the disc between $r_d = 2$ and 6 , required to model the strong, elongated red wing, seems to require the primary emission concentrated close to this area of the disc, as in models *A* and *C* with small r_s or h_s . Similarly, such an enhanced illumination occurs in model S_K with small r_s . For a single primary source, in model S_K , the best agreement with parameters from Fabian et al. (2002) is achieved for $r_s \lesssim 2$, Fig. 18(e). For larger r_s , the model predicts profiles possessing the red tail with a pronounced bumpy feature (cf. Figs. 6(b,c)), which is not seen in the time-averaged profile of the observed line. On the other hand, superposition of profiles corresponding to various r_s smooths out the shape of the red wing, see Fig. 19. Then, we explore below in some details a model with variability effects resulting primarily from the change of the distance, r_s , at which dominant contribution of hard X-rays is produced and with the time-averaged spectrum formed by superposition of spectra corresponding to various r_s .

Motivated by variability effects, discussed in the next section, we focus on model S_K^{PT} and we constrain the range of distances to $r_s \leq 3$, which range is relevant to modelling the variability. Moreover, significant contribution from $r_s \gtrsim 3$ would yield the blue peak broader than the observed one, at least for limb-darkened $I(\mu_{\text{em}})$, see below. The detailed

shape of the superposition profile depends (weakly for the considered range of r_s , see below) on relative magnitudes of contribution from various r_s . These, in turn, result from both the dependence of intrinsic luminosity on r_s , which is fixed in model S_K^{PT} , and the length of time at which emission is generated at various r_s . The latter should correspond to the length of periods spent by the source in various flux states.

The light curve for the 2001 observation (figure 12 from Vaughan & Fabian 2004) indicates that the source spends most of the time in intermediate flux states, with rare transitions to the very low state and more frequent, but very short, periods of higher flux states. We identify the lowest flux states with $r_s < 1.8$ (see Section 4.6) and the highest flux states with $r_s \approx 3$. Then, the most frequent, intermediate flux states would correspond to $r_s \approx 2 - 2.4$. These would yield the difference by a factor of ~ 1.5 between direct fluxes of primary emission in the intermediate and high flux states.

As illustrated in Fig. 19, the detailed shape of the line is weakly sensitive to specific distribution of r_s , provided that the distribution involves a few positions within $r_s = 2.2 - 3$ (contributions from these larger r_s are shown in panels (a) and (b)), so that the red wing is smoothed out. In next sections we consider model S_K^{PT} involving $r_s = 1.8, 2, 2.2, 2.5$ and 3 (denoted below as D_1), for which the superposition profile reproduces the observed line, see Fig. 20(a). Furthermore, this distribution of r_s approximates the distribution of flux states indicated by the light-curve, with higher fluxes less frequently sampled, more closely than a uniform distribution of r_s (denoted as D_2). Note, however, that for the uniform distribution D_2 only a weak excess between 4 and 5 keV occurs with respect to D_1 , see Fig. 19(b). These two distributions of r_s yield also similar equivalent widths (EW_{tot} , see Section 4.4) of the Fe line, namely 670 and 620 eV for D_1 and D_2 , respectively.

Individual profiles of lines for small r_s (≤ 2) differ weakly from each other as well as from the profile of the superposition, see Fig. 19(c). Therefore, the superposition profile is insensitive to details of contribution from small r_s , e.g., the profiles for $r_s = 1.5 - 3$ and $1.8 - 3$ are almost identical (Fig. 19(c)). This property is more thoroughly explored in Section 4.6.

Superposition of lines from sources located at $r_s \leq 3$ reproduces shape of the observed line at $E < 5$ keV (see Fig. 20(a,b)) for both limb-darkened and limb-brightened emission. On the other hand, details of modelling the line at higher energies depend on angular emissivity law. The strong blue peak, at $E > 5.5$ keV, has to be formed by photons originating mostly from the inner disc rather than from a distant material. Vaughan & Fabian (2004) find that the width of the peak requires the emitting region to be located at $r_d \sim 30$. However, they use a non-relativistic formula for the Doppler effect, therefore that value gives an upper limit on the distance of that region. With a fully relativistic modelling, we find that the peak may be reproduced with the major contribution coming from $r_d \sim 10$. For $I(\mu_{\text{em}}) \propto 1 + 2.06\mu_{\text{em}}$, illumination of that region by sources located within $r_s = 1.8 - 3$ is approximately sufficient to yield the peak with the observed strength, the solid curve in Fig. 20(a). On the other hand, for this $I(\mu_{\text{em}})$, strong emission from $r_s = 4 - 10$ would overproduce the line flux

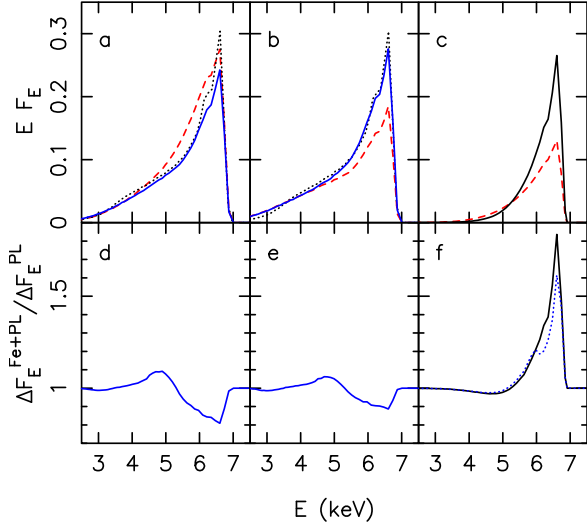


Figure 20. The dotted (black) curves in (a) and (b) show profile of the Fe line with parameters of the best fit from Fabian et al. (2002), same as in Fig. 18. (a) The solid (blue) and dashed (red) curve shows the superposition profile for primary X-ray sources distributed in the range $r_s = 1.8 - 3$ (D_1 ; same as the solid curves in Fig. 19) and $r_s = 1.8 - 20$, respectively, in model S_K^{PT} with $I(\mu_{em}) \propto 1 + 2.06\mu_{em}$. (b) The solid (blue) and dashed (red) curve shows superposition profile for primary X-ray sources distributed in the range $r_s = 1.8 - 3$ (D_1) in model S_K^{PT} with $I(\mu_{em}) \propto \log(1 + 1/\mu_{em})$. The solid curve includes additional contribution from the source located close to the axis at $r_s = 10$ (model $[S_K^{PT}, A]$, see text). (c) The solid and dashed curve shows profile for $h_s = 8$ and 4 , respectively, in model C with $I(\mu_{em}) \propto 1 + 2.06\mu_{em}$. The bottom panels show the difference spectra corresponding to models shown in top panels. (d) The difference between spectra for $r_s = 3$ and $r_s = 1.8$ in model S_K^{PT} with $I(\mu_{em}) \propto 1 + 2.06\mu_{em}$. (e) Same as in (d) but for $I(\mu_{em}) \propto \log(1 + 1/\mu_{em})$. (f) The solid (black) curve shows the difference between spectra for $h_s = 8$ and 4 in model C with $I(\mu_{em}) \propto 1 + 2.06\mu_{em}$. The dotted (blue) curve is for $I(\mu_{em}) = I_0$ and $r_{out} = 100$ as in Miniutti et al. (2003).

in 5-6 keV range, yielding too large width of the line core, the dashed curve in Fig. 20(a).

For $I(\mu_{em}) \propto \log(1 + 1/\mu_{em})$, primary sources described by model S_K^{PT} are not sufficient to reproduce the strength of the blue peak, see the dashed curve in Fig. 20(b). In this case, an additional primary source illuminating the disc mostly at $r_d \simeq 10$, e.g. a source at $r_s \simeq 10$ at the symmetry axis, is required to reproduce the blue peak. In next sections we discuss some properties for the specific case of sources described by model S_K^{PT} with $r_s = 1.8 - 3$ and an additional source, described by model A with $r_s = 10$ and $V = 0$, emitting 10 per cent of total X-ray luminosity. This model, denoted below as $[S_K^{PT}, A]$, yields the time-averaged profile in very good agreement with the observed one, see the solid curve in Fig. 20(b).

4.2 Variability

A model consisting of a strongly variable, in normalisation, power-law and a more constant reflection component explains variability of MCG-6-30-15 measured by *ASCA* (Shih et al. 2002) and *XMM-Newton* (e.g., Fabian & Vaughan

2003). Specifically, figure 5 in Fabian & Vaughan (2003) shows changes of magnitude of reflection by a factor of $\lesssim 2$ corresponding to changes of the primary radiation by a factor of 5.

Such reduction of variability could be entirely explained by GR effects for a source, with constant intrinsic luminosity, described by model S_K and changing the radial distance within $r_s = 2 - 3$, see the solid curve in Fig. 7(a). In this case, however, variations of the line, although reduced, would be correlated with those of the primary radiation. On the other hand, Fabian & Vaughan (2003) do not reveal any such trend in variations of both components. Then, it seems that modelling of the observed variability should involve changes of the intrinsic luminosity with r_s . Specifically, model S_K^{PT} with $r_s = 1.8 - 3$, yielding approximately constant reprocessed flux for the primary flux varying by a factor of 3, appears to be the most feasible to explain that variability pattern.

Additional changes, by a factor of $\lesssim 2$, of the intrinsic luminosity at a given r_s would be required in model S_K^{PT} to account for the spread of reprocessed flux values for a specific value of the primary flux. Alternatively, such variations of the reprocessed component, at fixed primary component, could be explained by changes of h_s , as for $h_s < 1$ such variations of the height yield an almost constant primary flux and the Fe flux varying by a factor of 2, see the dotted curve in Fig. 7(a).

The reduction effect is weakened if even a small fraction of X-rays is generated at larger distances, as required by the time-averaged profile for limb-brightened $I(\mu)$, see Fig. 20(b). E.g., for model $[S_K^{PT}, A]$, involving a constant source, located at $r_s = 10$ at the axis and emitting 10 per cent of total X-ray luminosity, variations of the distance of a source described by S_K^{PT} within $r_s = 1.8 - 3$ yield the change the observed primary flux by a factor of 2 (at the constant Fe flux).

A similar reduction, by a factor of 2, of the Fe flux variations is predicted in model A as well as in model C , interestingly, in both cases in the range of parameters relevant for modelling the time-averaged profile. Namely, in model A , this effect - involving enhancement by returning radiation, see Section 3.5.1 - occurs for small r_s , for which the line with strong red wing is produced, cf. Fig. 18(d). In model C , reduced variations of the Fe flux - basing on specific $V(h_s)$ - occur for the intermediate heights, for which the model fits the observed profile according to Miniutti et al. (2003). On the other hand, neither of these models is able to explain some finer details of spectral variability revealed in the rms spectra, see below. Note that effects related to light-travel time are (at most) marginally important in these applications of models A and C to MCG-6-30-15. In particular, for $h_s < 8$ in model C , fraction of Fe photons from $r_d > 150$ is smaller than 5 per cent and the longest delay time (corresponding to a small fraction of photons coming from the farthest, to observer, side of the disc) for photons reflected from $r_d = 150$ is smaller than 3.5 ks (for $M = 3 \times 10^6 M_\odot$).

Note also that the above is not the unique variability pattern observed in MCG-6-30-15. Namely, Reynolds et al. (2004) find that during the 2000 *XMM* observation, for the range of the 2-10 keV flux between $F_{2-10} = 2 \times 10^{-11}$ (the deep minimum level) and 4×10^{-11} erg/s/cm² (typical state), the line followed variations of the power-law component, keeping approximately constant equivalent width. This

is clearly a different behaviour than during the *ASCA* as well as the 2001 *XMM-Newton* observations when, in the same range of F_{2-10} , the line did not vary, leading to strongly reflection dominated spectra at low-flux states (e.g. Iwasawa 1996, Fabian & Vaughan 2003, see also figs. 13 and 14 in Vaughan & Fabian 2004). This indicates that the nature of the physical mechanism underlying variability during the 2000 observation is different than that of other observations. A plausible interpretation involves assumption that, in the former, variability was primarily due to variations of intrinsic luminosity while in other cases it was dominated by GR effects.

The rms spectra for the 2001 *XMM* observation reveal the suppressed variability around 6.5 keV, see e.g. figure 16 in Vaughan & Fabian (2004). Such suppression could be due to the presence of reflection from distant material, as suggested for explanation of similar features in the rms spectra of several other objects (see, e.g., Ponti et al. 2006). In MCG-6-30-15, however, contribution of such a constant spectral component is very weak (see Lee et al. 2002, Iwasawa et al. 1996). Therefore, the suppressed variability of the blue peak of the line should be explained within the GR variability model. As discussed in Section 3.6, only model S_K^{PT} (or S_K) is able to explain such property. Moreover, the decline around 6.5 keV in the rms spectrum occurs in the range of r_s for which the model reproduces the time-averaged profile.

On the other hand, Vaughan & Fabian (2004) indicate hints for increased variability around the Fe line energy in the rms spectrum for lower flux states, although ambiguities remain in interpretation of that analysis (see their figures 16 and 17 and discussion in section 5.3.2). We emphasise that such property, if confirmed, would contradict predictions of model S_K^{PT} , where a slightly stronger decline in the rms spectrum should correspond to lower luminosity states, see Fig. 15. Then, in the framework of model S_K^{PT} , such property would require stronger variations of intrinsic luminosity, at a fixed r_s , for smaller r_s .

Ponti et al. (2004) note an excess of fractional variability in the 4.7-5.8 keV band (followed by a drop at energies close to 6.4 keV) in the rms spectrum of the 2000 observation, suggesting presence of a spectral component which varies more than the underlying continuum. Such an excess may result from variations of the red wing of the line corresponding to changes of the position within $r_s = 2 - 4$, see Fig. 14(c).

4.3 Time-resolved profiles; difference spectra

High-quality spectra for time-scales on which the flux remains approximately constant should reveal line profiles corresponding to a fixed position of the X-ray source. Specifically, for model S_K^{PT} these profiles should exhibit clear bumpy features in the red wing. MCG-6-30-15 varies strongly on time-scales < 1 ks. Current data allow to determine spectra for time bins of at least 10 ks. Then, these spectra would involve averaging over certain ranges of r_s in model S_K^{PT} , which in turn would smooth out the red wing (see also Fig. 22(c)). We note, however, clear indications of bumps in the line profile below 6 keV in the *ASCA* observations and some, less significant, hints in the *XMM-Newton* data. If interpreted in terms of model S_K^{PT} predictions, this

would indicate that in some cases generation of X-rays is localised around specific r_s on timescales ≥ 10 ks.

The time-averaged profile of 1999 *ASCA* observation (see figure 1 in Shih et al. 2002) has a main peak at ~ 6.5 keV and then an additional peak at $\gtrsim 5$ keV (qualitatively similar but less pronounced peaks around 5 keV are seen in time averaged profiles from 1994 and 1997 *ASCA* observations; see Tanaka et al. 1995 and Iwasawa et al. 1999). This profile is modelled with a rather flat radial emissivity, $q \lesssim 3$, and a small outer radius, in the range $r_{out} = 10-30$. For such parameters, the lower energy peak is formed in the way illustrated in Fig. 11(c). However, that fitting model requires some complex geometry of the central region, with obscuration of more distant parts of the disc, justifying the above values of r_{out} ; otherwise, even a single point-like source in the central region would illuminate more distant regions of the disc, giving rise to a rather smooth profile, without the peak at 5 keV. On the other hand, the observed profiles may be explained by increased X-ray activity at $r_s \approx 3$ in model S_K^{PT} , without assuming such small values of r_{out} .

Such clear features are not revealed by *XMM-Newton* for similar flux states. However, the time-resolved (in 10 ks bins) spectra often show some features at $(2-3)\sigma$ level around 3.5-4 keV in the 2000 observation (see figure 8 in Reynolds et al. 2004; note that the time-average profile in that figure has a clear bump with maximum at $\lesssim 4$ keV) and around 4.5-5 keV in the 2001 observation (see figure 18 in Vaughan & Fabian 2004). Finally, Dovčiak et al. (2004a) note features near $E \sim 4.8$ keV in the time-averaged line profile of 2001 observation, which could be interpreted as a Doppler horn resulting from locally enhanced emission on some part of the disc. The above energies would correspond to $r_s \approx 2$ and 3 for the 2000 and 2001 observation, respectively.

Given a rather poor quality of the time-resolved spectra, less direct approaches to investigate spectral changes are made. Specifically, the difference spectra between various flux levels are determined, which show only the variable component of the spectrum, while the non-variable component is subtracted away. Figure 15 in Vaughan & Fabian (2004) shows the difference spectrum between the average spectra, for the whole 2001 observation, with fluxes lower and higher than the mean. The difference is consistent with a power-law, with residuals from the power-law model not exceeding 10 per cent. Therefore, it indicates very weak change of the spectrum of the reprocessed component. This property strongly challenges the GR models of variability, which in general predict rather significant changes of the line profile resulting from the change of the source position. Below we present example difference spectra for models S_K^{PT} and C .

We note, however, that both the low and high flux spectra in the analysis in Vaughan & Fabian (2004) involve averaging over wide ranges of flux states, see their figure 12, and the average fluxes for high and low flux spectra differ by a factor of 1.5. In GR variability models, such averaging would correspond to averaging over large ranges of r_s . Taking into account that, e.g., model S_K^{PT} should involve variations of intrinsic luminosity by a factor of $\lesssim 2$, these ranges of r_s may largely overlap. The most interesting constraint on spectrum presumably corresponding to an approximately fixed position is discussed in Section 4.6.

Figs. 20(d-f) show difference between spectra for $r_s = 3$ and $r_s = 1.8$ (i.e. between extreme positions considered above for the time-averaged profile) in model S_K^{PT} and for $h_s = 8$ and $h_s = 4$ in model C . The difference between the total spectra (Fe line + power-law) is divided by the difference of the primary power-laws. Variable red wing gives rise to an excess at $\lesssim 5$ keV, not exceeding 10 per cent. The exact energy of this excess depends on the value of r_s attributed to the high state, with higher energies corresponding to larger r_s . Owing to effects discussed in Section 3.5.2, model S_K^{PT} is characterised by relatively small variations of the blue peak. Deviations of the difference spectrum from a power-law, at the peak energy, depend on the angular emissivity law, with limb-brightened laws giving rise to smaller deviation.

In models A and C significantly stronger variations of the blue peak occur, therefore, these models predict much larger residuals around 6 keV (than model S_K^{PT}) in the difference of spectra between positions corresponding to low and high fluxes, see Fig. 20(f). Note also that significant deviations from power-law may occur in the difference between two profiles which fit the same observation equally well, see the dotted curve in Fig. 20(f), cf. Miniutti et al. (2003).

The difference spectrum between the 2001 and 2000 *XMM* observations shows an excess at 6.6 keV, see figure 20 in Vaughan & Fabian 2004, which could be due to a change in the flux of the blue peak of the Fe line. Such a change of the blue peak, yielding appropriate level of residuals around 6.6 keV, could result from significant change of the source height, as illustrated in Fig. 20(f), with the 2001 observation corresponding to larger h_s . On the other hand, this interpretation would not be consistent with other properties of the 2001 observation, discussed in this paper, which seem to require small h_s . Moreover, the line in the difference between the 2001 and 2000 observations is narrow, while that resulting from the change of h_s would be rather broad, with significant flux below 6 keV.

4.4 Equivalent width

High values of both the equivalent width (EW) of the Fe line and the normalisation parameter of Compton reflection ($R = \Omega/2\pi$), characterising the X-ray spectrum of MCG-6-30-15, are supposed to result from enhancement of disc irradiation by GR effects. Slightly different values of EW for the 2001 observation result from the two *XMM-Newton* detectors. Specifically, using the same model (with $R = 1$), Fabian et al. (2002) and Fabian & Vaughan (2003) find $EW = 550$ eV and $EW = 685$ eV using the data from MOS and pn camera, respectively. Allowing for higher normalisation of reflection, $R = 2.2$, Fabian et al. (2002) obtain $EW = 410$ eV. Using the *BeppoSAX* data, Ballantyne, Fabian & Vaughan (2003) find a high value of reflection parameter, $R > 2.6$, in agreement with the above EW values.

Note that procedure of computing the EW is particularly important in GR models. Specifically, for high R , the EW with respect to the sum of the power-law and Compton reflection, denoted below as EW_{tot} , may be much smaller than the EW with respect to the power-law only, denoted as EW_{PL} (see also examples of EW values for various procedures of computing in Miniutti et al. 2004).

We have determined both EW_{tot} and EW_{PL} (all values given below correspond to $\theta_{obs} = 30^\circ$). The latter may

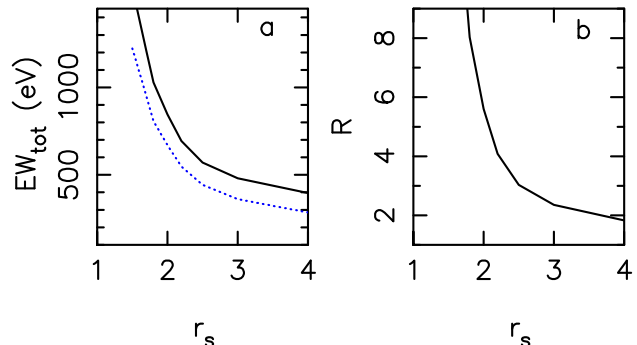


Figure 21. The solid curve in panel (a) and (b) shows the line EW (with respect to power-law + reflection continuum) and the reflection parameter, respectively, as a function of the source distance r_s , for S_K^{PT} with $I(\mu_{em}) \propto 1 + 2.06\mu_{em}$. The reflection parameter is determined as $R = EW_{PL}/EW_{PL}^{class}$, see text, with $EW_{PL}^{class} = 260$ eV. The dotted (blue) curve is for $I(\mu_{em}) \propto \log(1 + 1/\mu_{em})$

be used, by comparing with the classical value (i.e. for the model with no relativistic effects), EW_{PL}^{class} , to estimate the reflection normalisation parameter as $R = EW_{PL}/EW_{PL}^{class}$. The value of EW_{PL}^{class} depends on the angular emission law, in accordance with changes of the line profile discussed in Section 3.7. E.g., $EW_{PL}^{class} = 170$ and 260 eV corresponds to $I(\mu_{em}) \propto \log(1 + 1/\mu_{em})$ and $I(\mu_{em}) \propto 1 + 2.06\mu_{em}$, respectively. Neglecting the factor 1.3 (related with elemental abundance, see Section 2), we find $EW_{PL}^{class} = 130$ eV (in agreement with George & Fabian 1991; see their figure 14) for $I(\mu_{em}) \propto \log(1 + 1/\mu_{em})$. However, dependence of R on specific $I(\mu_{em})$ is rather weak; differences between limb-brightened and limb-darkened cases do not exceed 20 per cent. In Fig. 21(b) we show values of R corresponding to limb-darkened $I(\mu_{em})$, which is closer to angular dependence of Compton reflected component.

In model S_K^{PT} with small r_s , the EW_{tot} is extremely sensitive to r_s , see Fig. 21(a). For $I(\mu_{em}) \propto 1 + 2.06\mu_{em}$, the EW_{tot} increases from 480 to 1030 eV with the distance decreasing from $r_s = 3$ to 1.8. The superposition of sources within $r_s = 1.8 - 3$ (D_1 , the solid curve in Fig. 20(a)) yields $EW_{tot} = 670$ eV. For $I(\mu_{em}) \propto \log(1 + 1/\mu_{em})$, in the same range of r_s , EW_{tot} increases from 360 to 800 eV, and the superposition yields $EW_{tot} = 520$ eV. Then, for the limb-brightened $I(\mu_{em})$, EW_{tot} is in approximate agreement with spectral fits of the *XMM-Newton* data. The limb-darkened $I(\mu_{em})$ yields a slightly higher value, although this conclusion is affected by uncertain abundance of iron.

The reflection parameter for the superposition of sources within $r_s = 1.8 - 3$ in model S_K^{PT} is $R = 3.8$, which value is within the confidence limit from analysis of the *BeppoSAX* data in Ballantyne et al. (2003).

The EW is significantly reduced if even a small fraction of X-rays is emitted at larger distances, as required by the time-averaged profile for limb-brightened $I(\mu_{em})$. E.g., an additional source at the axis, $r_s = 10$, in model $[S_K^{PT}, A]$ (the solid curve in Fig. 20(b)), emitting 10 per cent of the X-ray luminosity, yields $EW_{tot} = 380$ eV and $R \lesssim 3$.

4.5 X-ray luminosity

The primary emission, observed at small θ_{obs} , is strongly reduced in model S_K^{PT} for the range of distances relevant to modelling of the line profile and variability effects. In particular, for $r_s = 3$ and 1.8, it is reduced by a factor of 8 and 70, respectively. Then, the observed hard X-ray flux would be reduced by over an order of magnitude due to GR effects. The 2–10 keV flux in the typical state of MCG–6–30–15 corresponds to isotropic luminosity $L_{2-10}^{\text{iso}} = 4 \times 10^{42}$ erg/s, implying the total isotropic luminosity $L_X^{\text{iso}} \lesssim 2 \times 10^{43}$ erg/s. The above reduction factors imply that the intrinsic luminosity of the X-ray source is $L_X \simeq 2 \times 10^{44}$ erg/s $\approx 0.5 L_{\text{Edd}}$ (for $M = 3 \times 10^6 M_\odot$) and this in turn indicates $\dot{M} \gtrsim \dot{M}_{\text{Edd}}$, making the central engine of MCG–6–30–15 closely similar to those of Narrow Line Seyfert 1 galaxies (e.g. Collin & Kawaguchi 2004).

The NIR/optical/UV luminosity (presumably thermal emission of an optically thick disc) is estimated to $L_{\text{disc}} \geq 2 \times 10^{43}$ erg/s by Reynolds et al. (1997). The above lower limit corresponds to the minimum reddening allowed for MCG–6–30–15. The putative rapid rotation of the black hole implies that the thermal disc emission, driven either by direct dissipation of the accretion power or by irradiation by X-rays, should emerge mostly from distances of a few R_g . Then, the disc emission would be subject to similar reduction as the X-rays and therefore the disc luminosity may be comparable to that of the X-ray source (or higher for larger values of the reddening). Actually, this scenario, i.e. a more luminous disc emission beamed along the equatorial plane, is consistent with very high luminosity of MIR/FIR radiation coming from reprocessing of central emission, see discussion in Reynolds et al. (1997).

4.6 Low flux state

The lowest flux states, with spectra dominated by the reflection component, are particularly interesting for studying the strongly relativistic regime of space-time. In the GR models, these states would correspond to positions of the X-ray source in the immediate vicinity of the event horizon. Properties of the lowest flux spectra seem to deviate between various observations of MCG–6–30–15.

The line profile of the deep minimum state analysed by Iwasawa et al. (1996) is completely dominated by the red wing, while the blue peak is strongly suppressed. This could be interpreted as the result of generation of primary emission at small r_s close to the axis (i.e. in the regime of model A rather than S), however, some challenge for this model results from enhancement of the blue peak by illumination of the surrounding disc (i.e. beyond a few R_g) by returning radiation.

Indeed, such a line profile, dominated by the red wing, can be modelled with very steep ϵ_{Fe} profiles ($q > 4$) on the whole disc, so that contribution from beyond a few R_g is negligible. As a result, the line is formed in bulk by strongly redshifted photons and has a bumpy shape without a blue peak. A similar (more extreme) effect is considered as the reason of non-detection of a broad line in some spectra presumed to be affected by strong GR effects, e.g. NGC 4051 (see e.g. figure 7 and the related discussion in Miniutti & Fabian 2004). In principle, such lines may result from *direct*

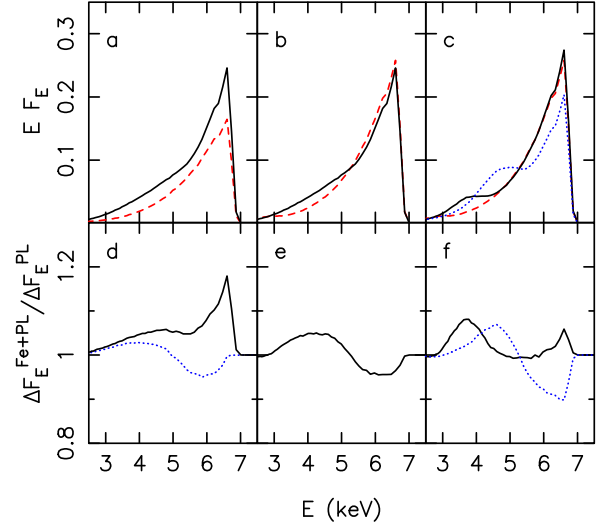


Figure 22. The figure shows the difference between spectra of higher flux states, averaged over some ranges of source position, and the lowest flux state, for a fixed source position, in model S_K^{PT} with $I(\mu_{\text{em}}) \propto 1 + 2.06\mu_{\text{em}}$. The solid (black) curves in panel (a) and (b) show superposition of profiles for $r_s = 1.8-3$, same as the solid curve in Fig. 20(a). The solid (black) and dotted (blue) curve in (c) shows superposition for $r_s = 2-2.2$ and $2.5-3$, respectively. The dashed (red) curves show profiles for the superposition and for the single source position are adjusted so that they correspond to equal times of observation. The solid (black) curves in panels (d-f) and the dotted (blue) curve in (f) show the difference spectra (the lower flux spectrum subtracted from the higher flux spectrum) for parameters indicated for the top panels. The dotted (blue) curve in panel (d) is for the same parameters as the solid one but with the spectrum for $r_s = 1.5$ multiplied by a factor of 1.5.

illumination by a source, with $V = 0$, at a very small r_s close to the symmetry axis. However, in any such model, additional illumination by the returning radiation would result in generation of a rather pronounced blue peak. The above effect does not occur if the reflecting (optically thick) material is absent within at least $2R_g$.

Reynolds et al. (2004) argue that the lack of the blue peak is the characteristic property of the low state. However, some low flux profiles do have strong blue peak, see below, on the other hand, a profile with no blue peak was revealed during the flare in the 1997 *ASCA* observation (Iwasawa et al. 1999). Note also that the analysis in Reynolds et al. (2004) involves a wide range of flux states including much higher than that of the deep minimum. Moreover, their fits include a narrow Fe line with $\text{EW} = 100$ eV, which value is much higher than these typically found for this object (e.g. Iwasawa et al. 1996, Lee et al. 2002).

Finally, we argue that properties of the low flux state of the 2001 observation, analysed by Fabian & Vaughan (2003), are consistent with predictions of model S_K^{PT} . The spectrum of that state is strongly dominated by reflection, with very large $\text{EW} = 1.4$ keV, similar as for the deep minimum of the *ASCA* observation. On the other hand, the profile has a strong blue peak, as implied both by consistency with higher flux profiles, see below, and by the fit with $q = 3.3$ and high r_{out} . To account for such high values of EW, model S_K^{PT} requires the X-rays to be emitted from $r_s \leq 1.7$. For these r_s ,

the observed primary X-ray flux is reduced by a factor of $\gtrsim 100$, in approximate agreement with normalisation of the power-law component for low flux state in figure 5 in Fabian & Vaughan (2003). Note that for these r_s the strongly irradiated part of the disc, under the source, does not contribute to the line profile - due to extreme redshift and reduction of this emission. Then, the line can be modelled by a single radial power-law, with $q \approx 3$, in agreement with the fit from Fabian & Vaughan (2003). Such line profile does not possess any bumpy features in the red wing and is similar to the profile averaged over the range of r_s corresponding to higher flux states. This property is consistent with those derived from analyses of the 2001 observation, as discussed below.

The light curve for the 2001 observation in general exhibits rapid variability, except for a rather prolonged period ($\gtrsim 10$ ks) of the lowest flux state, see bin 303:k in figure 2 from Fabian & Vaughan (2003). Weak changes of the flux suggest that this period may correspond to a fixed location of the source. Remarkably, spectrum from this period is similar to spectrum averaged over some range of higher fluxes; see figure 3 in Fabian & Vaughan (2003) with up to 20 per cent residuals in the difference spectrum. Similar property is found in Fabian et al. (2002) for another low flux period; Vaughan & Fabian (2004) note that they do not find evidence for strong systematic residuals in the difference spectra between the lowest flux state and several higher flux levels.

Fig. 22 shows the difference spectra between the flux states, averaged over some ranges of r_s , and the lowest flux state, predicted in model S_K^{PT} for limb-darkened angular emissivity - which gives rise to the largest deviations in the difference spectra. For $r_s = 1.7$, the residuals are small, approximately within the observational constraints. For very small r_s , model S_K^{PT} predicts decrease of the line flux, cf. Fig. 7(c), therefore, $r_s = 1.5$ the residuals are relatively large. However, the shape of the line is similar to the averaged profile and a slight modification of the model, yielding higher line flux, reduces the residuals to a small level, see the dotted curve in Fig. 22(d).

Note that in two Narrow Line Seyfert 1 galaxies, NGC 4051 and 1H 0707-495, properties of the lowest flux state are different than predicted by model S_K^{PT} . In these objects, the reflected component is correlated with the primary power-law at low flux values and becomes more constant at higher fluxes (Fabian et al. 2004, Ponti et al. 2006). Similarly as for the 2000 observation of MCG-6-30-15, significant changes of intrinsic luminosity would be required to explain those low flux states.

4.7 Discussion

Model S_K^{PT} , with $a = 0.998$, seems to be the most feasible to explain these properties of the X-ray spectrum of MCG-6-30-15 which are supposed to result from GR effects. Below we summarise predictions of the model which are consistent with the observed properties

- (i) Primary emission from sources distributed within $r_s = 1.8 - 3$ gives rise to the line profile possessing a red wing consistent with that revealed in the 2001 observation.
- (ii) Changes of the distance of the source, within $r_s = 1.8 - 3$, yield variations of the primary emission flux with constant

normalisation of reflection component.

- (iii) Change of the distance, within $r_s = 1.8 - 3$, gives rise to a decline in the rms spectrum at 6.5 keV.

- (iv) Primary emission from a source located at $r_s \leq 1.7$ produces a strongly reflection dominated spectrum, consistent with that observed in the lowest flux states; moreover, the line profile for such location is similar to the average profile for larger r_s .

- (v) Rather significant changes of the line profile occur when the distance of a single source changes at $r_s > 2$; the resulting, systematic residuals in the difference spectra are, however, relatively small (~ 20 per cent level) and the model reproduces reasonably well a power-law like difference spectrum.

Some details of the model, e.g. modelling of the blue peak or the EW value, depend on the angular emission law.

Note that model S_K , with some modifications, could explain a smoothed red wing even without superposition, i.e. for a single source at $r_s = 2 - 3$. Moreover, such model could account for small changes of the line profile corresponding to the change of r_s . Namely, photons forming the variable, bumpy part of the red wing may be depleted due to ionization of the disc surface, neglected in this paper. Qualitatively, the strongest ionization should occur under the source, where the photons forming the redshifted horns originate. We emphasise that if future observations confirm that the line profile remains strictly unchanged at any flux level, applicability of model S would indeed require strong reduction of fluorescent emission from the region under the source, involving ionization of that region.

Another possibility to suppress the bumps in the red wing involves generation of X-rays at a slightly larger h_s , for which a more extended area under the source is illuminated and the wing does not possess a pronounced feature, compare Figs. 18(e) and 18(f).

Our model S_K^{PT} represents most closely a model with flares occurring randomly at various distances. In a realistic scenario, the X-rays would be always generated by flares distributed over a range of r_s and the observed Fe profile would correspond to the superposition of profiles for a single r_s . Variability effects would then result from changes of the distance of the strongest activity. These changes of r_s giving the dominating contribution should result in changes of the line profile described above. We note, however, a caveat for the model with flares. Namely, the model involving compact sources corotating with the disc predicts quasi-periodic modulation of the primary emission because of Doppler effect as the source circles around the centre (see Życki & Niedźwiecki 2005). This signal would appear on the Keplerian time scale, which is shorter than time scales considered in this paper. However, such a signal is not observed in the *XMM-Newton* data from MCG-6-30-15 (Vaughan, Fabian & Nandra 2003). This may imply a continuous spacial distribution of the hard X-ray source, e.g. an extended corona covering the disc surface or a small hot torus replacing the disc, in both cases within a few innermost R_g (as needed for the variability effects).

5 DISCUSSION AND CONCLUSIONS

5.1 Variability models

We have extended the model, formulated by Miniutti & Fabian (2004), relating reduced variability of the reflected emission to changing magnitude of relativistic effects as location of the primary X-ray source changes. We find that original computations of Miniutti & Fabian (2004) - for a model involving a vertically moving source - overestimate the reduction effect by assuming a value of the outer radius of the disc which is too small for the range of the source heights considered in that model.

On the other hand, we find a significant reduction of the variability of reflected emission in a model with a rapidly rotating black hole and a source moving radially, low above the disc surface. The reduced variability occurs then for the innermost range of radial distances, $\leq 4R_g$. We find also that - only in this range of parameters - the GR effects give rise to a significant decline around 6.5 keV in rms spectra.

Note that generation of strong X-ray emission at these distances ($\leq 4R_g$) is consistent with the condition of a high value of a , as - for a rapidly rotating black hole - most accretion power is dissipated within a few innermost R_g .

5.2 The black hole spin

Determination of the value of black hole spin or, even more fundamentally, verification of effects predicted by the Kerr metric solution of GR equations - remains a major issue of black hole astrophysics. In this context, several effects are taken into account for X-ray spectroscopy. Strong redshift of photons forming the observed red wings, at $E < 4$ keV, is considered as evidence of rapid rotation of a black hole (e.g., Brenneman & Reynolds 2006). However, similar redshift can be obtained for $a = 0$ if emission from $r_d < 6$ is taken into account (Reynolds & Begelman 1997). Then, the derived high value of a relies on assumption of no neutral iron emission from within the radius of marginal stability.

Response of the line to increase of primary emission has been suggested for future studies. In particular, Reynolds et al. (1999) indicate a bump occurring in the line profile and progressing to lower energies, with proceeding time, as a feature characteristic for a rapidly rotating black hole. Again, a similar - redshifted and Shapiro delayed - bump should appear for a non-rotating black hole if fluorescence inside r_{ms} was taken into account.

A straightforward analysis of the space-time metric could be performed for systems observed close to edge-on, for which effects due to lensing by a black hole would be directly seen in the line profile (e.g., Zakharov & Repin 2003). However, as noted in Narayan & McClintock (2005), there seems to be a selection effect preventing such systems from being observed.

Then, we point out that a (largely unambiguous) analysis of imprints of the space-time metric would be possible in profile of the line resulting from irradiation by a strong flare just above the disc surface. If such a flare occurred at $r_s \lesssim 4$, properties of the space-time related with the black hole rotation would result in $\gtrsim 10$ per cent in magnitude effects in the line profile. The effects related to the value of a are rather subtle but in principle possible to establish

observationally. A compact flare dominating total emission would be required to make such an analysis feasible and viability of such scenario is uncertain. Such flares are indeed occasionally observed (e.g., Ponti et al. 2004). Interestingly, however, the Fe K α line was actually very weak during the flare analysed by Ponti et al. (2004), and a strong line appeared in the spectrum with significant time delay after the flare.

Finally, we emphasise that the reduced variability of reflected component - basing on mechanism advocated in this paper - is itself a direct manifestation of the nature of the Kerr space-time. Note that another effect resulting from properties of the Kerr metric, namely anisotropic emission of hard X-rays generated close to a rotating black hole, is qualitatively consistent with inclination-angle dependence of intrinsic spectra of Seyfert galaxies (Niedźwiecki 2005). In support for the tentative relation of these two effects to properties of the Kerr metric, note also that comparison of the total mass in black holes in the local universe with the total luminosity produced by active galactic nuclei indicates that most supermassive black holes should rotate rapidly, e.g. Elvis, Risaliti & Zamorani (2002).

5.3 Modelling the red wing of relativistic Fe lines

As discussed above, detection of photons with $E < 4$ keV is considered as the evidence of rapid rotation of the black hole. Such strongly redshifted photons were revealed in the Fe line profiles observed in MCG-6-30-15 and several other objects (e.g., Miller et al. 2004, Miniutti et al. 2004). When fitted by models assuming a power-law radial emissivity, the observed profiles require $q > 4$ within $(6-10)R_g$. Considering physical scenarios for generation of such profiles, we find that they

(i) can be produced as a result of illumination by a hard X-ray source located close to a black hole (preferably at $r_s = 2-3$) and rather close to the disc surface ($h_s \lesssim 1$);

(ii) cannot be explained by models involving a source at a height of several R_g , or higher, close to the axis;

if they are to come from a disc, with small inclination, surrounding a rotating black hole. Regarding (ii) we find, in agreement with previous studies, that such location of the source yields a steep ϵ_{Fe} , with $q > 3$, in the innermost part of the disc. However, this steep ϵ_{Fe} occurs only within $r_d \leq 2$ (and due to gravitational blueshift rather than light bending). The majority of emission from this region of the disc is either captured or bent toward the disc plane; moreover, the observed photons are strongly redshifted. As a result, this emission gives only a minor contribution to the line profile and it is not relevant to the shape and strength of the observed red wings. This conclusion is not affected by effects related with azimuthal motion of the source, returning radiation or angular emission law of fluorescence; these effects influence mostly the strength of the blue peak. On the other hand, the red wing is primarily related with position of the X-ray source.

5.4 Returning radiation, non-local irradiation

A further challenge for modelling certain line profiles results from illumination of the surrounding disc (i.e. beyond

a few R_g) by returning radiation. We find that this effect may be strong for the range of parameters (small r_s and V) previously not explored. A similarly strong enhancement of Compton reflection by returning radiation, for very small distances ($r_s \lesssim 2$) of primary source, was noted recently by Suebsewong et al. (2006).

Another effect, related to bending of photon trajectories to the disc plane, affects models relating the Fe radial profile to some physical processes. These models typically assume that the radial profile of Fe emission is the same as some physically motivated profile of energy dissipation. E.g., Reynolds et al. (2004) make such assumption in their analysis of the *XMM* observation of MCG-6-30-15, applying model of the torqued-disc emission (where emission results mostly from extraction of rotational energy of the black hole and thus is very centrally concentrated). Moreover, they assume that there is no dissipation, and thus no reprocessing, beyond rather small (several R_g) outer radius. We emphasise that even for X-rays generated very low above the disc surface, a significant illumination of more distant regions of the disc should occur.

Both the returning radiation and the non-locality of irradiation result primarily in enhancement of the blue peak of the line.

5.5 Azimuthal motion

Impact of strong gravity is usually studied under specific assumptions on the X-ray source motion. Typically, angular velocity of the source is related to that of the disc (e.g. Ruszkowski 2000; Miniutti & Fabian 2004), while Dabrowski & Lasenby (2001) assume a static primary source. We note that change of V significantly affects flux and profile of the iron line through combination of SR and GR effects. Moreover, the Kerr metric terms yield a non-trivial dependence between V and Ω (equation (8)). Then, the assumed parametrisation of motion may be crucial for derived properties, e.g. in some variability models. Obviously, additional effects may result from relativistic vertical or radial motion of the source (e.g. Yu & Lu 2001), which were neglected in this paper.

5.6 Applicability of our results

We focused above on MCG-6-30-15, for which several observed properties may be explained by our model. Similar effects, including reduced variability of reflection, pronounced red wings or strongly reflection dominated spectra, have been revealed in some Narrow Line Seyfert 1 galaxies (e.g. Fabian et al. 2004; Ponti et al. 2006), as well as in stellar mass black-hole systems (e.g. Miniutti et al. 2004) and in galactic nuclei with much higher black hole masses (Fabian et al. 2005). Note that our scenario implies that the X-ray luminosity is underestimated by an order of magnitude in these objects.

On the other hand, most black-hole systems do not show signatures of such extreme effects. Then, similar reduction of the X-ray flux does not necessarily characterise any low inclination system. Note, however that such property would be inevitable for rapidly rotating black holes, where major fraction of accretion power is dissipated at very small r_s , if this power is converted into hard X-rays in situ.

As in virtually all previous studies of that subject, we analysed impact of GR effects for the simplest case of an isotropic point source of hard X-ray emission, which approach follows from our lack of understanding of the X-ray source nature. The derived properties result from transfer of radiation from source to disc and observer and from disc to observer. Additional (but smaller in magnitude) effects may occur in more realistic models. E.g., Comptonization close to a Kerr black hole gives rise to anisotropic emission, cf. Niedźwiecki (2005), therefore radiation with different spectral index may irradiate various parts of the disc, while the transfer effects affect only normalisation and cut-off energy of the primary emission.

The simplified description of X-ray source considered in this paper approximates most closely scenario with magnetic flares above the disc surface. Then, our results may be directly applicable to a model with flares occurring randomly at various radial distances. Qualitatively, we may assess similar variability effects for continuous spacial distributions of the hard X-ray source, e.g. an extended corona covering the disc surface or a small hot torus replacing the disc within a few innermost R_g . Varying size of such an extended, hot plasma, in the Kerr metric, should give rise reduced variability of reflected component. In particular, a decline of direct emission from a shrinking corona or torus would be observed, even if its intrinsic luminosity remained unchanged, while increasing fraction of its emission would be bent to the disc plane giving rise to strong reflection component.

The major shortcoming in our study results from the neglect of ionization effects. The strongest ionization should occur below the source, especially in models with low height above the disc surface. In general, strong ionization of this region should suppress the redshifted Doppler horns formed in the red-wing. On the one hand, this would make studies of effects related to value of a less feasible. On the other hand, such depletion of the variable contribution to the red wing would reduce variations of the line profile at various flux states. However, details of ionization structure, and of the related reduction of the variable contribution to the line, depend on additional assumptions, in particular, on azimuthal distribution of flares. Obviously, a strong single flare would give rise to stronger ionization than many weak flares uniformly distributed at a given r_s .

5.7 Summary

If attributed to strong-gravity effects, both the time-averaged line profile and the variability pattern observed in MCG-6-30-15 by *XMM-Newton* independently indicate that a primary hard X-ray source must be located very close ($\lesssim 4R_g$) to a black hole, i.e. in the region where Kerr metric effects become crucial. Rapid rotation of the black hole is necessary (and vastly sufficient) to account for reduction of variability of reflected emission for such spacial location of the source. Bending to the equatorial plane, underlying this reduction effect, appears to be the most pronounced effect of the Kerr metric to be studied in the X-ray spectra of black-hole systems.

ACKNOWLEDGMENTS

We thank the anonymous referee for detailed comments and suggestions to improve the paper. This work was partly supported by grant no. 2P03D01225 and N203 011 32/1518 from the Polish Ministry of Science and Higher Education.

REFERENCES

- Agol E., Krolik J. H., 2000, *ApJ*, 528, 161
- Anders E., Ebihara M., 1982, *Geochimica et Cosmochimica Acta*, 46, 2363
- Anders E., Grevesse N., 1989, *Geochimica et Cosmochimica Acta*, 53, 197
- Ballantyne D. R., Vaughan S., Fabian A. C., 2003, *MNRAS*, 342, 239
- Bardeen J. M., Press, W. H., & Teukolsky, S. A., 1972, *ApJ*, 178, 347
- Beckwith K., Done C., 2004, *MNRAS*, 352, 353
- Brenneman L. W., Reynolds C. S., 2006, *ApJ*, 652, 1028
- Collin S., Kawaguchi T., 2004, *A&A*, 426, 797
- Cunningham C. T., 1975, *ApJ*, 202, 788
- Cunningham C. T., 1976, *ApJ*, 208, 534
- Czerny B., Różańska A., Dovčiak M., Karas V., Dumont A.-M., 2004, *A&A*, 420, 1
- Dabrowski Y., Fabian A. C., Iwasawa K., Lasenby A. N., Reynolds C. S., 1997, *MNRAS*, 288, L11
- Dabrowski Y., Lasenby A. N., 2001, *MNRAS*, 321, 605
- Dovčiak M., Karas V., Yaqoob T., 2004a, *ApJS*, 153, 205
- Dovčiak M., Bianchi S., Guainazzi M., Karas V., Matt G., 2004b, *MNRAS*, 350, 745
- Elvis M., Risaliti G., Zamorani G., 2002, *ApJ*, 565, L75
- Fabian A. C., Miniutti G., 2005, in *Kerr Spacetime: Rotating Black Holes in General Relativity*, in press [astro-ph/0507409]
- Fabian, A. C., Vaughan S., 2003, *MNRAS*, 340, L28
- Fabian A. C. et al., 2002, *MNRAS*, 335, L1
- Fabian A. C., Miniutti G., Gallo L., Boller Th., Tanaka Y., Vaughan S., Ross R. R., 2004, *MNRAS*, 353, 1071
- Fabian A. C., Miniutti G., Iwasawa K., Ross R. R., 2005, *MNRAS*, 361, 795
- George I. M., Fabian A. C., 1991, *MNRAS*, 249, 352
- Goyder R., Lasenby A. N., 2004, *MNRAS*, 353, 338
- Iwasawa et al. 1996, *MNRAS*, 282, 1038
- Iwasawa K., Fabian A. C., Young A. J., Inoue H., Matsumoto C., 1999, *MNRAS*, 306, L19
- Laor A., 1991, *ApJ*, 376, 90
- Laor A., Netzer H., 1989, *MNRAS*, 238, 897
- Lee J. C., Iwasawa K., Houck J. C., Fabian A. C., Marshall H. L., Canizares C. R., 2002, *ApJ*, 570, L47
- Lu Y., Yu Q., 2001, *ApJ*, 561, 660
- Martocchia A., Karas V., Matt G., 2000, *MNRAS*, 312, 817
- Martocchia A., Matt G., 1996, *MNRAS*, 282, L53
- Martocchia A., Matt G., Karas V., 2002, *A&A*, 383, L23
- Mathews W. G., 1982, *ApJ*, 258, 425
- Matt G., Perola G. C., Piro L., Stella L., 1992, *A&A*, 257, 63
- McHardy I. M., Gunn K. F., Uttley P., Goad M. R., 2005, *MNRAS*, 359, 1469
- Miller J. M. et al., 2002, *ApJ*, 570, L69
- Miller J. M. et al., 2004, *ApJ*, 606, L131
- Miniutti G., Fabian A. C., Goyder R., Lasenby A. N., 2003, *MNRAS*, 344, L22
- Miniutti G., Fabian A. C., 2004, *MNRAS*, 349, 1435
- Miniutti G., Fabian A. C., Miller J. M., 2004, *MNRAS*, 351, 466
- Narayan R., McClintock J. E., 2005, *ApJ*, 623, 1017
- Nayakshin S., Kazanas D., 2002, *ApJ*, 567, 85
- Niedźwiecki A., 2005, *MNRAS*, 356, 913
- Page D. N., Thorne K. S., 1974, *ApJ*, 191, 499
- Pecháček T., Dovčiak M., Karas V., Matt G., 2005, *A&A*, 441, 855
- Petrucci P. O., Henri G., 1997, *A&A*, 326, 99
- Ponti G., Cappi M., Dadina M., Malaguti G., 2004, *A&A*, 417, 451
- Ponti G., Miniutti G., Cappi M., Maraschi L., Fabian A. C., Iwasawa K., 2006, *MNRAS*, 368, 903
- Reynolds C. S., Begelman M. C., 1997, *ApJ*, 488, 109
- Reynolds C. S., Fabian A. C., 1997, *MNRAS*, 290, L1
- Reynolds C. S., Nowak M. A., 2003, *Physics Reports*, 377, 389
- Reynolds C. S., Ward M. J., Fabian A. C. Celotti A., 1997, *MNRAS*, 291, 403
- Reynolds C. S., Young A. J., Begelman M. C., Fabian A. C., 1999, *ApJ*, 514, 164
- Reynolds C. S., Wilms J., Begelman M. C., Staubert R., Kendziorra E., 2004, *MNRAS*, 349, 1153
- Ruszkowski M. 2000, *MNRAS*, 315, 1
- Shih D. C., Iwasawa K., Fabian A. C., 2002, *MNRAS*, 333, 687
- Stella L., 1990, *Nature*, 344, 747
- Suebsuwong T., Malzac J., Jourdain E., Marcowith A., 2006, *A&A*, 453, 773
- Tanaka Y. et al., 1995, *Nature*, 375, 659
- Vaughan S., Fabian A. C., 2004, *MNRAS*, 348, 1415
- Vaughan S., Fabian A. C., Nandra K., 2003, *MNRAS*, 339, 1237
- Wilms J., Reynolds C. S., Begelman M. C., Reeves J., Molendi S., Staubert R., Kendziorra E., 2001, *MNRAS*, 328, L27
- Young A. J., Ross R. R., Fabian A. C., 1998, *MNRAS*, 300, L11
- Yu Q., Lu Y., 2000, *MNRAS*, 311, 161
- Zakharov A. F., Repin S. V., 2003, *A&A*, 406, 7
- Życki P. T., Czerny B., 1994, *MNRAS*, 266, 653
- Życki P. T., Niedźwiecki A., 2005, *MNRAS*, 359, 308